Icarus 217 (2012) 714–739

Contents lists available at ScienceDirect

Icarus

journal homepage: www.elsevier.com/locate/icarus

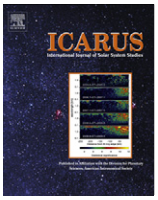

Sulfur chemistry in the middle atmosphere of Venus

Xi Zhang [a,*], Mao Chang Liang [b,c,d], Franklin P. Mills [e,f], Denis A. Belyaev [g,h], Yuk L. Yung [a]

[a] *Division of Geological and Planetary Sciences, California Institute of Technology, Pasadena, CA 91125, USA*
[b] *Research Center for Environmental Changes, Academia Sinica, Taipei, Taiwan*
[c] *Graduate Institute of Astronomy, National Central University, Zhongli, Taiwan*
[d] *Institute of Astronomy and Astrophysics, Academia Sinica, Taipei, Taiwan*
[e] *RSPE/AMPL, Mills Rd., Australian National University, Canberra, ACT 0200, Australia*
[f] *Fenner School of Environment and Society, Australian National University, Canberra, ACT 0200, Australia*
[g] *LATMOS, CNRS/INSU/IPSL, Quartier des Garennes, 11 bd. d'Alembert, 78280 Guyancourt, France*
[h] *Space Research Institute (IKI), 84/32 Profsoyuznaya Str., 117997 Moscow, Russia*

ARTICLE INFO

Article history:
Available online 14 July 2011

Keywords:
Venus, Atmosphere
Atmospheres, Chemistry
Photochemistry
Atmospheres, Composition

ABSTRACT

Venus Express measurements of the vertical profiles of SO and SO_2 in the middle atmosphere of Venus provide an opportunity to revisit the sulfur chemistry above the middle cloud tops (~58 km). A one dimensional photochemistry-diffusion model is used to simulate the behavior of the whole chemical system including oxygen-, hydrogen-, chlorine-, sulfur-, and nitrogen-bearing species. A sulfur source is required to explain the SO_2 inversion layer above 80 km. The evaporation of the aerosols composed of sulfuric acid (model A) or polysulfur (model B) above 90 km could provide the sulfur source. Measurements of SO_3 and SO ($a^1\Delta \rightarrow X^3\Sigma^-$) emission at 1.7 μm may be the key to distinguish between the two models.

1. Introduction

Venus is a natural laboratory of sulfur chemistry. Due to the difficulty of observing the lower atmosphere, we are still far from unveiling the chemistry at lower altitudes (Mills et al., 2007). On the other hand, the relative abundance of data above the middle cloud tops (~58 km) allows us to test the sulfur chemistry in the middle atmosphere. Mills et al. (2007) summarized the important observations before Venus Express and gave an extensive review of the sulfur chemistry on Venus.

Recently, measurements of Venus Express and ground-based observations have greatly improved our knowledge of the sulfur chemistry. Marcq et al. (2005, 2006, 2008) reported the latitudinal distributions of CO, OCS, SO_2 and H_2O in the 30–40 km region. The anti-correlation of latitudinal profiles of CO and OCS implies the conversion of OCS to CO in the lower atmosphere (Yung et al., 2009). Using the latitudinal and vertical temperature distribution obtained by Pätzold et al. (2007), Piccialli et al. (2008) deduced the dynamic structure, which shows a weak zonal wind pattern above ~70 km. The discovery of the nightside warm layer by the Spectroscopy for Investigation of Characteristics of the Atmosphere of Venus (SPICAV) onboard Venus Express (Bertaux et al., 2007) is a strong evidence of substantial heating in the lower thermosphere (above 90 km). Near the antisolar point, this heating is consistent with the existence of a subsolar–antisolar (SSAS) circulation. However, the nightside warm layer has been reported in SPICAV observations at all observed local times and latitudes and does not appear to be consistent with ground-based submillimeter observations (Clancy et al., 2008). Through the occultation technique, Solar Occultation at Infrared (SOIR) and SPICAV carry out measurements of the vertical profiles of major species above 70 km, including H_2O, HDO, HCl, HF (Bertaux et al., 2007), CO (Vandaele et al., 2008), SO and SO_2 (Belyaev et al., 2008, 2012). Aerosols are found to be in a bimodal distribution above 70 km (Wilquet et al., 2009). These high vertical resolution profiles are obtained mainly in the polar region. Using the SPICAV nadir mode, Marcq et al. (2011a) found large temporal and spatial variations of the SO_2 column densities above the cloud top in the period of 2006–2007, which suggests that the cloud region is dynamically very active. Ground-based measurements also provide valuable information. Krasnopolsky (2010a, 2010b) obtained spatially resolved distributions of CO_2, CO, HDO, HCl, HF, OCS, and SO_2 at the cloud tops from the CSHELL spectrograph at NASA/IRTF. Sandor et al. (2010) reported ground-based submillimeter observations of SO and SO_2 inversion layers above 85 km. The submillimeter results are qualitatively consistent with the vertical profiles from Venus Express (Belyaev et al., 2012). However, only the smallest SO and SO_2 abundances inferred from the SPICAV observations (Belyaev et al., 2012) are quantitatively similar to those inferred from the submillimeter observations (Sandor et al., 2010). Spatial and temporal variability may explain at least some of the differences among the observations (Sandor et al., 2010), but detailed inter-comparisons are required. These measurements and the proposed correlation of

---

* Corresponding author.
E-mail address: xiz@gps.caltech.edu (X. Zhang).

0019-1035/$ - see front matter © 2011 Elsevier Inc. All rights reserved.
doi:10.1016/j.icarus.2011.06.016

upper mesosphere SO_2 abundances with temperature open up new opportunities to study the photochemical and transport processes in the middle atmosphere of Venus.

Sandor et al. (2010) found that SO and SO_2 inversion layers cannot be reproduced by the previous photochemical model (Yung and DeMore, 1982). Therefore they suggested that the photolysis of sulfuric acid aerosol might directly produce the gas phase SO_x. A detailed photochemical simulation by Zhang et al. (2010) showed that the evaporation of H_2SO_4 aerosols with subsequent photolysis of H_2SO_4 vapor could provide the major sulfur source in the lower thermosphere if the rate of photolysis of H_2SO_4 vapor is sufficiently high. Their models also predicted supersaturation of H_2SO_4 vapor pressure around 100 km. The latest SO and SO_2 profiles retrieved from the Venus Express measurements agree with their model results (Belyaev et al., 2012). This mechanism reveals the close connection between the gaseous sulfur chemistry and aerosols. Previously sulfuric acid was considered only as the ultimate sink of gaseous sulfur species in the middle atmosphere. If it could also be a source, the thermodynamics and microphysical properties of H_2SO_4 must be examined more carefully. Alternatively, if the polysulfur (S_x) is indeed a significant component of the aerosols as the unknown UV absorber, Carlson (2010) estimated that the elemental sulfur is about 1% of the H_2SO_4 abundance. This might also be enough to produce the sulfur species if there is a steady supply of S_x aerosols to the upper atmosphere.

The purpose of this paper is to use photochemical models to investigate the sulfur chemistry in the middle atmosphere and its relation with aerosols based on our current knowledge of observational evidence and laboratory measurements. We will introduce our model in Section 2. In Section 3, we will discuss the two possible sulfur sources above 90 km, H_2SO_4 and S_x, respectively, the roles they play in the sulfur chemistry, their implications and how to distinguish the two sources by the future observations. The last section provides a summary of the paper and conclusions.

2. Model description

Our photochemistry-diffusion model is based on the one dimensional Caltech/JPL kinetics code for Venus (Yung and DeMore, 1982; Mills, 1998) with updated chemical reactions. The model solves the coupled continuity equations with chemical kinetics and diffusion processes, as functions of time and altitude from 58 to 112 km. The atmosphere is assumed to be in hydrostatic equilibrium. We use 32 altitude grids with increments of 0.4 km from 58 to 60 km and 2 km from 60 to 112 km. The diurnally averaged radiation field from 100 to 800 nm is calculated using a modified radiative transfer scheme including gas absorption, Rayleigh scattering by molecules and Mie scattering by aerosols with wavelength-dependent optical properties (see Appendix A). The unknown UV absorber is approximated by changing the single scattering albedo of the mode 1 aerosols beyond 310 nm, as suggested by Crisp (1986). Because the SO, SO_2 and aerosol profiles from Venus Express are observed in the polar region during the solar minimum period (2007–2008), our calculations are set at a circumpolar latitude (70°N) and we use the low solar activity solar spectra for the duration of the Spacelab 3 ATMOS experiment with an overlay of Lyman alpha as measured by the Solar Mesospheric Explorer (SME).

In this study we selected 51 species, namely, O, $O(^1D)$, O_2, $O_2(^1\Delta)$, O_3, H, H_2, OH, HO_2, H_2O, H_2O_2, N_2, Cl, Cl_2, ClO, HCl, HOCl, ClCO, $COCl_2$, ClC(O)OO, CO, CO_2, S, S_2, S_3, S_4, S_5, S_7, S_8, SO, $(SO)_2$, SO_2, SO_3, S_2O, HSO_3, H_2SO_4, OCS, OSCl, $ClSO_2$, four chlorosulfanes (ClS, ClS_2, Cl_2S, and Cl_2S_2) and eight nitrogen-containing species (N, NO, NO_2, NO_3, N_2O, HNO, HNO_2, and HNO_3). The chlorosulfanes (S_mCl_n) are included because they open an important pathway to form S_2 and polysulfur $S_{x(x=2\rightarrow8)}$ in the region 60–70 km (Mills and Allen, 2007), although there are significant uncertainties in their chemistry. The chlorosulfane chemistry is not important for the sulfur cycles above ~80 km because the S_mCl_n abundances are low. Nitrogen-containing species, especially NO and NO_2, can act as catalysts for converting SO to SO_2 and O to O_2 in the 70–80 km region (Krasnopolsky, 2006). A recent study by Sundaram et al. (2011) suggests that the odd nitrogen (NO_x) chemistry might also have significant effects on the abundances of sulfur oxides in the 80–90 km region.

In Zhang et al. (2010), the chemistry was simplified because $(SO)_2$, S_2O and HSO_3 were considered only as the sinks of the sulfur species. This might not be accurate enough for the chemistry below 80 km where there seems to be difficulty in matching the SO_2 observations. Instead, a full set of 41 photodissociation reactions is used here, along with about 300 neutral chemical reactions, as listed in Tables 1 and 2 respectively. We take the ClCO thermal equilibrium constant from the 1-sigma model in Mills et al. (2007) so that we can constrain the total O_2 column abundances to $\sim 2 \times 10^{18}\,cm^{-2}$. In addition, we introduce the heterogeneous nucleation processes of elemental sulfur (S, S_2 and polysulfur) because these sulfur species can readily stick to sulfuric acid droplets and may provide the source material for the unknown UV absorber (Carlson, 2010). But we neglect all the heterogeneous reactions among the condensed elemental sulfur species on the droplet surface. The calculation of the heterogeneous condensation rates is described in Appendix B. The accommodation coefficient α is varied from 0.01 to 1 for the sensitivity study (Section 4).

The temperature profiles are shown in Fig. 1 (left panel). The daytime temperature profile below 100 km (solid line) is obtained from the observations of VeRa onboard Venus Express near the polar region (71°N, Fig. 1 of Pätzold et al., 2007). Above 100 km the temperature is from Seiff (1983). The nighttime temperature profile (dashed line) above 90 km is measured by Venus Express in orbit 104 at latitude 4°S and local time 23:20 h (black curve in Fig. 1 of Bertaux et al. (2007)). The nighttime temperature profile is used to calculate the H_2SO_4 saturation vapor pressure only.

In the 1-D model, species are assumed to be mixed vertically by turbulent eddies. Molecular diffusion becomes important above the homopause region (~130–135 km). The eddy diffusivity increases with altitude in the Venus mesosphere for reasons discussed later. Since the zonal wind is observed to decrease with altitude above 70 km due to the temperature gradient from pole to equator (Piccialli et al., 2008), we assume that vertical transport of gas species is predominantly due to mixing caused by transient internal gravity waves, as proposed by Prinn (1975). In this case the eddy diffusion coefficient will be inversely proportional to the square root of the number density (Lindzen, 1981). Von Zahn et al. (1980) derived the eddy diffusion coefficient $\sim 1.4 \times 10^{13}\,[M]^{-0.5}\,cm^2\,s^{-1}$ from the number density around the homopause region, based on mass spectrometer measurements from *Pioneer Venus*. In our model we use slightly larger values $K_z = 2.0 \times 10^{13}\,[M]^{-0.5}\,cm^2\,s^{-1}$ above 80 km to include an additional contribution of the SSAS circulation. In the region below 80 km, Woo and Ishimaru (1981) estimated the diffusivity $\leqslant 4.0 \times 10^4\,cm^2\,s^{-1}$ at ~60 km from radio signal scintillations. Therefore our eddy diffusivity profile from 58 to 80 km is estimated by linear interpolation between the values at 80 and 60 km. The eddy diffusion profile is shown in Fig. 1 (right panel). However, the vertical advection due to the SSAS circulation might be dominant above 90 km. The SPICAV measurements show that the SO_2 mixing ratio from ~90 to 100 km is almost constant with altitude, which implies a very efficient transport process.

Since Zhang et al. (2010) has already shown that the model without additional sulfur sources above 90 km cannot explain the observed SO_2 inversion layer, we focus on two models in this

Table 1
Photolysis reactions.

	Reaction	Photolysis coefficient J (s^{-1})		Wavelength (nm)	Reference
		at 112 km	at 68 km		
R1	$O_2 + h\upsilon \rightarrow 2O$	8.8×10^{-8}	7.4×10^{-10}	$3 \leqslant \lambda \leqslant 242$	b
R2	$O_2 + h\upsilon \rightarrow O + O(^1D)$	2.1×10^{-7}	0	$117 \leqslant \lambda \leqslant 178$	b
R3	$O_3 + h\upsilon \rightarrow O_2 + O$	1.2×10^{-3}	2.3×10^{-3}	$158 \leqslant \lambda \leqslant 800$	a
R4	$O_3 + h\upsilon \rightarrow O_2(^1\Delta) + O(^1D)$	7.6×10^{-3}	1.1×10^{-2}	$53 \leqslant \lambda \leqslant 325$	a
R5	$O_3 + h\upsilon \rightarrow O_2 + O(^1D)$	2.3×10^{-6}	3.2×10^{-6}	$320 \leqslant \lambda \leqslant 325$	a
R6	$O_3 + h\upsilon \rightarrow O_2(^1\Delta) + O$	2.6×10^{-6}	3.2×10^{-6}	$120 \leqslant \lambda \leqslant 325$	a
R7	$O_3 + h\upsilon \rightarrow 3O$	9.2×10^{-7}	1.0×10^{-11}	$53 \leqslant \lambda \leqslant 203$	a
R8	$OH + h\upsilon \rightarrow O + H$	4.8×10^{-6}	0	$91 \leqslant \lambda \leqslant 193$	d
R9	$HO_2 + h\upsilon \rightarrow OH + O$	5.4×10^{-4}	7.0×10^{-4}	$190 \leqslant \lambda \leqslant 260$	c
R10	$H_2O + h\upsilon \rightarrow H + OH$	3.1×10^{-6}	0.0	$61 \leqslant \lambda \leqslant 198$	a
R11	$H_2O + h\upsilon \rightarrow H_2 + O(^1D)$	5.2×10^{-8}	0.0	$80 \leqslant \lambda \leqslant 143$	a
R12	$H_2O + h\upsilon \rightarrow 2H + O$	6.2×10^{-8}	0.0	$80 \leqslant \lambda \leqslant 143$	a
R13	$H_2O_2 + h\upsilon \rightarrow 2OH$	9.7×10^{-5}	1.3×10^{-4}	$120 \leqslant \lambda \leqslant 350$	a
R14	$Cl_2 + h\upsilon \rightarrow 2Cl$	2.6×10^{-3}	3.9×10^{-3}	$240 \leqslant \lambda \leqslant 475$	a
R15	$ClO + h\upsilon \rightarrow Cl + O$	6.2×10^{-3}	8.4×10^{-3}	$230 \leqslant \lambda \leqslant 325$	a
R16	$HCl + h\upsilon \rightarrow H + Cl$	1.9×10^{-6}	5.5×10^{-8}	$135 \leqslant \lambda \leqslant 232$	e
R17	$HOCl + h\upsilon \rightarrow OH + Cl$	4.6×10^{-4}	6.4×10^{-4}	$200 \leqslant \lambda \leqslant 380$	a
R18	$COCl_2 + h\upsilon \rightarrow 2Cl + CO$	5.1×10^{-5}	7.4×10^{-5}	$182 \leqslant \lambda \leqslant 285$	a
R19	$CO_2 + h\upsilon \rightarrow CO + O$	1.1×10^{-8}	4.3×10^{-13}	$120 \leqslant \lambda \leqslant 204$	a
R20	$CO_2 + h\upsilon \rightarrow CO + O(^1D)$	3.5×10^{-9}	0.0	$63 \leqslant \lambda \leqslant 160$	a
R21	$S_2 + h\upsilon \rightarrow 2S$	4.0×10^{-3}	5.8×10^{-3}	$238 \leqslant \lambda \leqslant 278$	b
R22	$S_3 + h\upsilon \rightarrow S_2 + S$	1.2	2.4	$350 \leqslant \lambda \leqslant 455$	b
R23	$S_4 + h\upsilon \rightarrow 2S_2$	2.2×10^{-1}	5.5×10^{-1}	$425 \leqslant \lambda \leqslant 575$	b
R24	$ClS + h\upsilon \rightarrow S + Cl$	2.6×10^{-2}	59×10^{-2}	$337 \leqslant \lambda \leqslant 500$	a
R25	$Cl_2S + h\upsilon \rightarrow ClS + Cl$	2.2×10^{-3}	3.9×10^{-3}	$190 \leqslant \lambda \leqslant 460$	a
R26	$ClS_2 + h\upsilon \rightarrow S_2 + Cl$	6.8×10^{-2}	1.4×10^{-1}	$327 \leqslant \lambda \leqslant 485$	a
R27	$SO + h\upsilon \rightarrow S + O$	3.7×10^{-4}	1.8×10^{-4}	$113 \leqslant \lambda \leqslant 232$	a
R28	$SO_2 + h\upsilon \rightarrow S + O_2$	1.5×10^{-6}	1.9×10^{-7}	$63 \leqslant \lambda \leqslant 210$	a*
R29	$SO_2 + h\upsilon \rightarrow SO + O$	2.0×10^{-4}	$7.2 \times 10–5$	$63 \leqslant \lambda \leqslant 220$	a
R30	$SO_3 + h\upsilon \rightarrow SO_2 + O$	3.6×10^{-5}	3.7×10^{-5}	$195 \leqslant \lambda \leqslant 300$	f
R31	$OCS + h\upsilon \rightarrow CO + S$	2.8×10^{-5}	4.2×10^{-5}	$185 \leqslant \lambda \leqslant 300$	a
R32	$H_2SO_4 + h\upsilon \rightarrow SO_3 + H_2O$	1.4×10^{-6}	1.4×10^{-7}	$121 \leqslant \lambda \leqslant 746$	g, h, i, j, k
R33	$S_2O + h\upsilon \rightarrow SO + S$	5.0×10^{-2}	6.2×10^{-2}	$260 \leqslant \lambda \leqslant 335$	a
R34	$ClC(O)OO + h\upsilon \rightarrow CO_2 + ClO$	5.3×10^{-3}	7.4×10^{-3}	$205 \leqslant \lambda \leqslant 305$	l
R35	$NO + h\upsilon \rightarrow N + O$	4.3×10^{-6}	0.0	$175 \leqslant \lambda \leqslant 195$	m
R36	$NO_2 + h\upsilon \rightarrow NO + O$	8.6×10^{-3}	1.5×10^{-2}	$120 \leqslant \lambda \leqslant 422$	m
R37	$NO_3 + h\upsilon \rightarrow NO_2 + O$	1.6×10^{-1}	4.4×10^{-1}	$410 \leqslant \lambda \leqslant 645$	n
R38	$NO_3 + h\upsilon \rightarrow NO + O_2$	2.4×10^{-2}	6.3×10^{-2}	$590 \leqslant \lambda \leqslant 645$	n
R39	$N_2O + h\upsilon \rightarrow N_2 + O(^1D)$	8.9×10^{-7}	3.0×10^{-3}	$100 \leqslant \lambda \leqslant 240$	m
R40	$HNO_2 + h\upsilon \rightarrow OH + NO$	1.9×10^{-3}	8.7×10^{-3}	$310 \leqslant \lambda \leqslant 390$	m
R41	$HNO_3 + h\upsilon \rightarrow NO_2 + OH$	1.2×10^{-4}	5.2×10^{-5}	$190 \leqslant \lambda \leqslant 350$	m

Note: The photolysis coefficient (J) in the units of s^{-1}refers to 112 km and 68 km at mid-latitude (45°N) with diurnal average (divided by 2).
References: (a) Mills (1998) and references therein; (b) Moses et al. (2002) and references therein; (c) Sander et al. (2006) and references therein; (d) Moses et al. (2000) and references therein; (e) Bahou et al. (2001); (f) Burkholder and McKeen (1997); (g) Vaida et al. (2003); (h) Mills et al. (2005); (i) Burkholder et al. (2000); (j) Hintze et al. (2003); (k) Lane and Kjaergaard (2008); (l) Pernice et al. (2004); (m) DeMore et al. (1994) and references therein; (n) DeMore et al. (1997) and references therein.

* Total SO_2 absorption cross sections between 227 and 420 nm are updated based on recent measurements by Hermans et al. (2009) and Vandaele et al. (2009).

Table 2
Chemical reactions.

	Reaction	Rate constant	Reference
R50	$O(^1D) + O_2 \rightarrow O + O_2$	$3.20 \times 10^{-11} e^{70./T}$	c
R51	$O(^1D) + N_2 \rightarrow O + N_2$	$1.80 \times 10^{-11} e^{110./T}$	c
R52	$O(^1D) + CO_2 \rightarrow O + CO_2$	$7.40 \times 10^{-11} e^{120./T}$	c
R53	$O_2(^1\Delta) + O \rightarrow O_2 + O$	2.00×10^{-16}	c
R54	$O_2(^1\Delta) + O_2 \rightarrow 2O_2$	$3.60 \times 10^{-18} e^{-220./T}$	c
R55	$O_2(^1\Delta) + H_2O \rightarrow O_2 + H_2O$	4.80×10^{-18}	c
R56	$O_2(^1\Delta) + N_2 \rightarrow O_2 + N_2$	1.00×10^{-20}	c
R57	$O_2(^1\Delta) + CO \rightarrow O_2 + CO$	1.00×10^{-20}	a
R58	$O_2(^1\Delta) + CO_2 \rightarrow O_2 + CO_2$	2.00×10^{-21}	Estimated
R59	$2O + CO_2 \rightarrow O_2 + CO_2$	$k_0 = 3.22 \times 10^{-28} T^{-2.0}$	Estimated
R60	$2O + CO_2 \rightarrow O_2(^1\Delta) + CO_2$	$k_0 = 9.68 \times 10^{-28} T^{-2.0}$	Estimated
R61	$2O + O_2 \rightarrow O_3 + O$	$k_0 = 5.90 \times 10^{-34} (T/300.)^{-2.4}$ $k_\infty = 2.80 \times 10^{-12}$	a
R62	$O + 2O_2 \rightarrow O_3 + O_2$	$k_0 = 5.90 \times 10^{-34} (T/300.)^{-2.4}$ $k_\infty = 2.80 \times 10^{-12}$	a
R63	$O + O_2 + N_2 \rightarrow O_3 + N_2$	$k_0 = 5.95 \times 10^{-34} (T/300.)^{-2.3}$ $k_\infty = 2.80 \times 10^{-12}$	a
R64	$O + O_2 + CO \rightarrow O_3 + CO$	$k_0 = 6.70 \times 10^{-34} (T/300.)^{-2.5}$ $k_\infty = 2.80 \times 10^{-12}$	a

Table 2 (*continued*)

	Reaction	Rate constant	Reference
R65	$O + O_2 + CO_2 \rightarrow O_3 + CO_2$	$k_0 = 1.40 \times 10^{-33}(T/300.)^{-2.5}$ $k_\infty = 2.80 \times 10^{-12}$	a
R66	$H + O_2 + N_2 \rightarrow HO_2 + N_2$	$k_0 = 5.70 \times 10^{-32}(T/300.)^{-1.6}$ $k_\infty = 7.50 \times 10^{-11}$	c
R67	$O + O_3 \rightarrow 2O_2$	$8.00 \times 10^{-12}e^{-2060./T}$	c
R68	$O(^1D) + O_3 \rightarrow 2O_2$	1.20×10^{-10}	c
R69	$O(^1D) + O_3 \rightarrow 2O + O_2$	1.20×10^{-10}	c
R70	$O_2(^1\Delta) + O_3 \rightarrow 2O_2 + O$	$5.20 \times 10^{-11}e^{-2840./T}$	c
R71	$H + O_3 \rightarrow OH + O_2$	$1.40 \times 10^{-10}e^{-470./T}$	c
R72	$OH + O_3 \rightarrow HO_2 + O_2$	$1.70 \times 10^{-12}e^{-940./T}$	c
R73	$OH + O_3 \rightarrow HO_2 + O_2(^1\Delta)$	$3.20 \times 10^{-14}e^{-940./T}$	a
R74	$HO_2 + O_3 \rightarrow OH + 2O_2$	$1.00 \times 10^{-14}e^{-490./T}$	c
R75	$O + H + M \rightarrow OH + M$	$k_0 = 1.30 \times 10^{-29}T^{-1.0}$	g
R76	$2H + M \rightarrow H_2 + M$	$k_0 = 2.70 \times 10^{-31}T^{-0.6}$	d
R77	$O + H_2 \rightarrow OH + H$	$8.50 \times 10^{-20}T^{2.7}e^{-3160./T}$	d
R78	$O(^1D) + H_2 \rightarrow H + OH$	1.10×10^{-10}	c
R79	$OH + H_2 \rightarrow H_2O + H$	$5.50 \times 10^{-12}e^{-2000./T}$	c
R80	$O + OH \rightarrow O_2 + H$	$2.20 \times 10^{-11}e^{120./T}$	c
R81	$H + OH + N_2 \rightarrow H_2O + N_2$	$k_0 = 6.10 \times 10^{-26}T^{-2.0}$	d
R82	$H + OH + CO_2 \rightarrow H_2O + CO_2$	$k_0 = 7.70 \times 10^{-26}T^{-2.0}$	d
R83	$2OH \rightarrow H_2O + O$	$4.20 \times 10^{-12}e^{-240./T}$	c
R84	$2OH + M \rightarrow H_2O_2 + M$	$k_0 = 6.20 \times 10^{-31}(T/300.)^{-1.0}$ $k_\infty = 2.60 \times 10^{-11}$	c
R85	$O + HO_2 \rightarrow OH + O_2$	$3.00 \times 10^{-11}e^{200./T}$	c
R86	$O + HO_2 \rightarrow OH + O_2(^1\Delta)$	$6.00 \times 10^{-13}e^{200./T}$	a
R87	$H + HO_2 \rightarrow 2OH$	7.21×10^{-11}	c
R88	$H + HO_2 \rightarrow H_2 + O_2$	7.29×10^{-12}	c
R89	$H + HO_2 \rightarrow H_2 + O_2(^1\Delta)$	1.30×10^{-13}	a
R90	$H + HO_2 \rightarrow H_2O + O$	1.62×10^{-12}	c
R91	$OH + HO_2 \rightarrow H_2O + O_2$	$4.80 \times 10^{-11}e^{250./T}$	c
R92	$OH + HO_2 \rightarrow H_2O + O_2(^1\Delta)$	$9.60 \times 10^{-13}e^{250./T}$	c
R93	$2HO_2 \rightarrow H_2O_2 + O_2$	$2.30 \times 10^{-13}e^{600./T}$	c
R94	$2HO_2 \rightarrow H_2O_2 + O_2(^1\Delta)$	$4.60 \times 10^{-15}e^{600./T}$	Estimated
R95	$2HO_2 + M \rightarrow H_2O_2 + O_2 + M$	$k_0 = 1.70 \times 10^{-33}e^{1000./T}$	c
R96	$O(^1D) + H_2O \rightarrow 2OH$	2.20×10^{-10}	c
R97	$O + H_2O_2 \rightarrow OH + HO_2$	$1.40 \times 10^{-12}e^{-2000./T}$	c
R98	$OH + H_2O_2 \rightarrow H_2O + HO_2$	$2.90 \times 10^{-12}e^{-160./T}$	c
R99	$Cl + O + M \rightarrow ClO + M$	$k_0 = 5.00 \times 10^{-32}$	e
R100	$Cl + O_3 \rightarrow ClO + O_2$	$2.30 \times 10^{-11}e^{-200./T}$	c
R101	$Cl + O_3 \rightarrow ClO + O_2(^1\Delta)$	$5.80 \times 10^{-13}e^{-260./T}$	c
R102	$Cl + H + M \rightarrow HCl + M$	$k_0 = 1.00 \times 0^{-32}$	e
R103	$Cl + H_2 \rightarrow HCl + H$	$3.70 \times 10^{-11}e^{-2300./T}$	c
R104	$Cl + OH \rightarrow HCl + O$	$8.33 \times 10^{-12}e^{-2790./T}$	h
R105	$Cl + HO_2 \rightarrow HCl + O_2$	$1.80 \times 10^{-11}e^{170./T}$	c
R106	$Cl + HO_2 \rightarrow OH + ClO$	$4.10 \times 10^{-11}e^{-450./T}$	c
R107	$Cl + H_2O_2 \rightarrow HCl + HO_2$	$1.10 \times 10^{-11}e^{-980./T}$	c
R108	$Cl + HOCl \rightarrow OH + Cl_2$	$6.00 \times 10^{-13}e^{-130./T}$	c
R109	$Cl + HOCl \rightarrow HCl + ClO$	$1.90 \times 10^{-12}e^{-130./T}$	c
R110	$Cl + ClCO \rightarrow Cl_2 + CO$	$2.16 \times 10^{-9}e^{-1670./T}$	h
R111	$Cl + CO + N_2 \rightarrow ClCO + N_2$	$k_0 = 1.30 \times 10^{-33}\ (T/300.)^{-3.8}$	a
R112	$Cl + OCS \rightarrow ClS + CO$	1.00×10^{-16}	c
R113	$Cl + ClS_2 \rightarrow S_2 + Cl_2$	1.00×10^{-12}	b
R114	$Cl + SO_2 + M \rightarrow ClSO_2 + M$	$k_0 = 1.30 \times 10^{-34}e^{940./T}$	a
R115	$2Cl + N_2 \rightarrow Cl_2 + N_2$	$k_0 = 6.10 \times 10^{-34}e^{900./T}$	a
R116	$2Cl + CO_2 \rightarrow Cl_2 + CO_2$	$k_0 = 2.60 \times 10^{-33}e^{900./T}$	a
R117	$O + Cl_2 \rightarrow ClO + Cl$	$7.40 \times 10^{-12}e^{-1650./T}$	a
R118	$O(^1D) + Cl_2 \rightarrow Cl + ClO$	1.55×10^{-10}	c
R119	$O(^1D) + Cl_2 \rightarrow Cl_2 + O$	5.25×10^{-11}	c
R120	$H + Cl_2 \rightarrow HCl + Cl$	$1.43 \times 10^{-10}e^{-590./T}$	a
R121	$OH + Cl_2 \rightarrow Cl + HOCl$	$1.40 \times 10^{-12}e^{-900./T}$	c
R122	$ClCO + Cl_2 \rightarrow COCl_2 + Cl$	$6.45 \times 10^{-12}\ k_{145}\ (170\alpha+[M])$	a
R123	$ClO + O \rightarrow Cl + O_2$	$3.00 \times 10^{-11}e^{70./T}$	c
R124	$ClO + O \rightarrow Cl + O_2(^1\Delta)$	$6.00 \times 10^{-13}e^{70./T}$	c
R125	$ClO + H_2 \rightarrow HCl + OH$	$1.00 \times 10^{-12}e^{-4800./T}$	c
R126	$ClO + OH \rightarrow HO_2 + Cl$	$7.40 \times 10^{-12}e^{270./T}$	c
R127	$ClO + OH \rightarrow HCl + O_2$	$6.00 \times 10^{-13}e^{230./T}$	c
R128	$ClO + HO_2 \rightarrow HOCl + O_2$	$2.70 \times 10^{-12}e^{220./T}$	c
R129	$ClO + CO \rightarrow CO_2 + Cl$	$1.00 \times 10^{-12}e^{-3700./T}$	c
R130	$2ClO \rightarrow Cl_2 + O_2$	$1.00 \times 10^{-12}e^{-1590./T}$	c
R131	$2ClO \rightarrow Cl_2 + O_2(^1\Delta)$	$2.00 \times 10^{-14}e^{-1590./T}$	c
R132	$ClO + OCS \rightarrow OSCl + CO$	2.00×10^{-16}	c
R133	$ClO + SO \rightarrow Cl + SO_2$	2.80×10^{-11}	c
R134	$ClO + SO_2 \rightarrow Cl + SO_3$	4.00×10^{-18}	c
R135	$ClO + SO_2 + M \rightarrow Cl + SO_3 + M$	$k_0 = 1.00 \times 10^{-35}$ $k_\infty = 4.00 \times 10^{-19}$	a

(*continued on next page*)

Table 2 (*continued*)

	Reaction	Rate constant	Reference
R136	$O + HCl \rightarrow OH + Cl$	$1.00 \times 10^{-11}e^{-3300./T}$	c
R137	$O(^1D) + HCl \rightarrow Cl + OH$	1.00×10^{-10}	c
R138	$O(^1D) + HCl \rightarrow ClO + H$	3.60×10^{-11}	c
R139	$O(^1D) + HCl \rightarrow O + HCl$	1.35×10^{-11}	c
R140	$OH + HCl \rightarrow Cl + H_2O$	$2.60 \times 10^{-12}e^{-350./T}$	c
R141	$O + HOCl \rightarrow OH + ClO$	1.70×10^{-13}	c
R142	$OH + HOCl \rightarrow H_2O + ClO$	$3.00 \times 10^{-12}e^{-500./T}$	c
R143	$O + ClCO \rightarrow Cl + CO_2$	3.00×10^{-11}	e
R144	$O + ClCO \rightarrow CO + ClO$	3.00×10^{-12}	e
R145	$ClCO + O_2 + M \rightarrow ClC(O)OO + M$	$k_0 = 5.70 \times 10^{-15}e^{500./T}/(10^{17} + 0.05\times[M])$	e
R146	$H + ClCO \rightarrow HCl + CO$	1.00×10^{-11}	e
R147	$OH + ClCO \rightarrow HOCl + CO$	1.50×10^{-10}	a
R148	$2ClCO \rightarrow COCl_2 + CO$	5.00×10^{-11}	a
R149	$ClCO + ClC(O)OO \rightarrow 2CO_2 + 2Cl$	1.00×10^{-11}	a
R150	$ClCO + N_2 \rightarrow CO + Cl + N_2$	$k_{eq} = 1.60 \times 10^{-25}e^{4000./T}$	a
R151	$O(^1D) + COCl_2 \rightarrow Cl_2 + CO_2$	3.60×10^{-10}	c
R152	$O(^1D) + COCl_2 \rightarrow ClCO + ClO$	3.60×10^{-10}	a
R153	$O + ClC(O)OO \rightarrow Cl + O_2 + CO_2$	1.00×10^{-11}	e
R154	$H + ClC(O)OO \rightarrow Cl + OH + CO_2$	1.00×10^{-11}	e
R155	$Cl + ClC(O)OO \rightarrow Cl + ClO + CO_2$	1.00×10^{-11}	e
R156	$2ClC(O)OO \rightarrow 2Cl + 2CO_2 + O_2$	5.00×10^{-12}	a
R157	$H + O_2 + CO_2 \rightarrow HO_2 + CO_2$	$k_0 = 2.00 \times 10^{-31}(T/300.)^{-1.6}$ $k_\infty = 7.50 \times 10^{-11}$	a
R158	$H + HCl \rightarrow H_2 + Cl$	$1.50 \times 10^{-11}e^{-1750./T}$	a
R159	$Cl + CO + CO_2 \rightarrow ClCO + CO_2$	$k_0 = 4.20 \times 10^{-33}(T/300.)^{-3.8}$	a
R160	$ClCO + CO_2 \rightarrow CO + Cl + CO_2$	$k_{eq} = 1.60 \times 10^{-25}e^{4000./T}$	a
R161	$O + CO + M \rightarrow CO_2 + M$	$k_0 = 1.70 \times 10^{-33}e^{-1510./T}$ $k_\infty = 2.66 \times 10^{-14}e^{-1459./T}$	g
R162	$O + 2CO \rightarrow CO_2 + CO$	$k_0 = 6.50 \times 10^{-33}e^{-2180./T}$	a
R163	$2O + CO \rightarrow CO_2 + O$	$k_0 = 3.40 \times 10^{-33}e^{-2180./T}$	a
R164	$OH + CO \rightarrow CO_2 + H$	1.50×10^{-13}	c
R165	$S + O + M \rightarrow SO + M$	$k_0 = 1.50 \times 10^{-34}e^{900./T}$	b
R166	$S + O_2 \rightarrow SO + O$	2.30×10^{-12}	i
R167	$SO + O \rightarrow SO_2 + O$	$1.60 \times 10^{-13}e^{-2280./T}$	k
R168	$HSO_3 + O_2\ HO_2 + SO_3$	$1.30 \times 10^{-12}e^{-330./T}$	c
R169	$ClS + O_2 \rightarrow SO + ClO$	2.00×10^{-15}	l
R170	$S + O_3 \rightarrow SO + O_2$	1.20×10^{-11}	c
R171	$SO + O_3 \rightarrow SO_2 + O_2$	$4.50 \times 10^{-12}e^{-1170./T}$	k
R172	$SO + O_3 \rightarrow SO_2 + O_2(^1\Delta)$	$3.60 \times 10^{-13}e^{-1100./T}$	c
R173	$SO_2 + O_3 \rightarrow SO_3 + O_2$	$3.00 \times 10^{-12}e^{-7000./T}$	c
R174	$SO_2 + O_3 \rightarrow SO_3 + O_2(^1\Delta)$	$6.00 \times 10^{-14}e^{-7000./T}$	Estimated
R175	$S + OH \rightarrow SO + H$	6.60×10^{-11}	c
R176	$S + HO_2 \rightarrow SO + OH$	$3.00 \times 10^{-11}e^{200./T}$	e
R177	$SO_3 + H_2O \rightarrow H_2SO_4$	$2.26 \times 10^{-43}\ Te^{-6544/T}\ [H_2O]$	j
R178	$ClS + Cl_2 \rightarrow Cl_2S + Cl$	7.00×10^{-14}	l
R179	$S + Cl + M \rightarrow ClS + M$	$k_0 = 1.00 \times 10^{-29}\ T^{-1.0}$	b
R180	$S + Cl_2 \rightarrow ClS + Cl$	$2.80 \times 10^{-11}e^{-290.T}$	l
R181	$S + ClO \rightarrow SO + Cl$	4.00×10^{-11}	b
R182	$S + ClCO \rightarrow CO + ClS$	3.00×10^{-12}	Estimated
R183	$S + ClCO \rightarrow OCS + Cl$	3.00×10^{-12}	Estimated
R184	$S + ClC(O)OO \rightarrow Cl + SO + CO_2$	3.00×10^{-11}	a
R185	$S + CO + M \rightarrow OCS + M$	$k_0 = 4.00 \times 10^{-33}e^{-1940./T}$	Estimated
R186	$2S + M \rightarrow S_2 + M$	$k_0 = 1.18 \times 10^{-29}$ $k_\infty = 1.00 \times 10^{-10}$	a
R187	$O + S_2 \rightarrow SO + S$	$2.20 \times 10^{-11}e^{-84./T}$	b
R188	$S + S_2 + M \rightarrow S_3 + M$	$k_0 = 1.00 \times 10^{-25}T^{-2.0}$ $k_\infty = 3.00 \times 10^{-11}$	a, b
R189	$ClO + S_2 \rightarrow S_2O + Cl$	2.80×10^{-11}	b
R190	$2S_2 + M \rightarrow S_4 + M$	$k_0 = 2.20 \times 10^{-29}$ $k_\infty = 1.00 \times 10^{-10}$	a
R191	$O + S_3 \rightarrow SO + S_2$	8.00×10^{-11}	b
R192	$S + S_3 \rightarrow 2S_2$	8.00×10^{-11}	b
R193	$S + S_3 + M \rightarrow S_4 + M$	$k_0 = 1.00 \times 10^{-25}T^{-2.0}$ $k_\infty = 3.00 \times 10^{-11}$	a, b
R194	$S_2 + S_3 + M \rightarrow S_5 + M$	$k_0 = 1.00 \times 10^{-25}T^{-2.0}$ $k_\infty = 3.00 \times 10^{-11}$	a, b
R195	$2S_3 + M \rightarrow S_6 + M$	$k_0 = 1.00 \times 10^{-30}$ $k_\infty = 3.00 \times 10^{-11}$	a
R196	$O + S_4 \rightarrow SO + S_3$	8.00×10^{-11}	b
R197	$Cl + S_4 \rightarrow ClS_2 + S_2$	2.00×10^{-12}	l
R198	$S + S_4 \rightarrow S_2 + S_3$	8.00×10^{-11}	b
R199	$S_3 + S_4 \rightarrow S_2 + S_5$	$4.00 \times 10^{-11}e^{-200./T}$	b
R200	$S + S_4 + M \rightarrow S_5 + M$	$k_0 = 1.00 \times 10^{-25}T^{-2.0}$ $k_\infty = 3.00 \times 10^{-11}$	a, b
R201	$S_2 + S_4 + M \rightarrow\ + M$	$k_0 = 1.00 \times 10^{-25}T^{-2.0}$	a, b

Table 2 (*continued*)

	Reaction	Rate constant	Reference
		$k_\infty = 3.00 \times 10^{-11}$	
R202	$S_3 + S_4 + M \rightarrow S_7 + M$	$k_0 = 1.00 \times 10^{-25} T^{-2.0}$ $k_\infty = 3.00 \times 10^{-11}$	a, b
R203	$S_4 + M \rightarrow 2S_2 + M$	$k_{eq} = 2.71 \times 10^{-27} e^{13100./T}$	f
R204	$2S_4 + M \rightarrow S_8 + M$	$k_0 = 1.00 \times 10^{-30}$ $k_\infty = 3.00 \times 10^{-11}$	a
R205	$O + S_5 \rightarrow S_4 + SO$	$8.00 \times 10^{-11} e^{-200./T}$	b
R206	$S + S_5 \rightarrow 2S_3$	$3.00 \times 10^{-11} e^{-200./T}$	b
R207	$S + S_5 \rightarrow S_2 + S_4$	$5.00 \times 10^{-11} e^{-200./T}$	b
R208	$S_3 + S_5 \rightarrow S_2 + S_6$	$4.00 \times 10^{-11} e^{-200./T}$	b
R209	$S_4 + S_5 \rightarrow S_2 + S_7$	$2.00 \times 10^{-12} e^{-200./T}$	b
R210	$S_4 + S_5 \rightarrow S_3 + S_6$	$2.00 \times 10^{-12} e^{-200./T}$	b
R211	$S + S_5 + M \rightarrow S_6 + M$	$k_0 = 1.00 \times 10^{-25}\ T^{-2.0}$ $k_\infty = 3.00 \times 10^{-11}$	a, b
R212	$S_2 + S_5 + M \rightarrow S_7 + M$	$k_0 = 1.00 \times 10^{-25}\ T^{-2.0}$ $k_\infty = 3.00 \times 0^{-11}$	a, b
R213	$S_3 + S_5 + M \rightarrow S_8 + M$	$k_0 = 1.00 \times 10^{-25} T^{-2.0}$ $k_\infty = 3.00 \times 10^{-11}$	a, b
R214	$O + S_6 \rightarrow S_5 + SO$	$8.00 \times 10^{-11} e^{-300./T}$	b
R215	$S + S_6 \rightarrow S_3 + S_4$	$3.00 \times 10^{-11} e^{-300./T}$	b
R216	$S + S_6 \rightarrow S_2 + S_5$	$5.00 \times 10^{-11} e^{-300./T}$	b
R217	$S_3 + S_6 \rightarrow S_2 + S_7$	$4.00 \times 10^{-12} e^{-300./T}$	b
R218	$S_4 + S_6 \rightarrow S_2 + S_8$	$2.00 \times 10^{-12} e^{-300./T}$	b
R219	$S_4 + S_6 \rightarrow 2S_5$	$2.00 \times 10^{-12} e^{-300./T}$	b
R220	$S + S_6 + M \rightarrow S_7 + M$	$k_0 = 1.00 \times 10^{-25}\ T^{-2.0}$ $k_\infty = 3.00 \times 10^{-11}$	a, b
R221	$S_2 + S_6 + M \rightarrow S_8 + M$	$k_0 = 1.00 \times 10^{-25}\ T^{-2.0}$ $k_\infty = 3.00 \times 10^{-11}$	a, b
R222	$S_6 + M \rightarrow 2S_3 + M$	$k_{eq} = 2.41 \times 10^{-29} e^{21483./T}$	f
R223	$O + S_7 \rightarrow S_6 + SO$	$8.00 \times 10^{-11} e^{-200./T}$	b
R224	$S + S_7 \rightarrow S_2 + S_6$	$4.00 \times 10^{-11} e^{-200./T}$	b
R225	$S + S_7 \rightarrow S_3 + S_5$	$2.00 \times 10^{-11} e^{-200./T}$	b
R226	$S + S_7 \rightarrow 2S_4$	$2.00 \times 10^{-11} e^{-200./T}$	b
R227	$S_3 + S_7 \rightarrow S_2 + S_8$	$3.00 \times 10^{-11} e^{-200./T}$	b
R228	$S_3 + S_7 \rightarrow S_4 + S_6$	$1.00 \times 10^{-11} e^{-200./T}$	b
R229	$S_3 + S_7 \rightarrow 2S_5$	$1.00 \times 10^{-11} e^{-200./T}$	b
R230	$S_4 + S_7 \rightarrow S_3 + S_8$	$5.00 \times 10^{-12} e^{-200./T}$	b
R231	$S_4 + S_7 \rightarrow S_5 + S_6$	$5.00 \times 10^{-12} e^{-200./T}$	b
R232	$S + S_7 + M \rightarrow S_8 + M$	$k_0 = 1.00 \times 10^{-25}\ T^{-2.0}$ $k_\infty = 3.00 \times 10^{-11}$	a, b
R233	$O + S_8 \rightarrow S_7 + SO$	$8.00 \times 10^{-11} e^{-400./T}$	b
R234	$S + S_8 \rightarrow S_2 + S_7$	$4.00 \times 10^{-11} e^{-400/T}$	b
R235	$S + S_8 \rightarrow S_3 + S_6$	$2.00 \times 10^{-11} e^{-400./T}$	b
R236	$S + S_8 \rightarrow S_4 + S_5$	$2.00 \times 10^{-11} e^{-400./T}$	b
R237	$S_2 + S_8 \rightarrow 2S_5$	$1.00 \times 10^{-11} e^{-1400./T}$	b
R238	$S_8 + M \rightarrow 2S_4 + M$	$k_{eq} = 1.17 \times 10^{-29} e^{22695./T}$	f
R239	$O + SO \rightarrow S + O_2$	$6.60 \times 10^{-13} e^{-2760./T}$	a
R240	$O + SO + M \rightarrow SO_2 + M$	$k_0 = 5.10 \times 10^{-31}$ $k_\infty = 5.30 \times 10^{-11}$	a*
R241	$OH + SO \rightarrow SO_2 + H$	8.60×10^{-11}	c
R242	$HO_2 + SO \rightarrow SO_2 + OH$	2.80×10^{-11}	Estimated
R243	$Cl + SO + M \rightarrow OSCl + M$	$k_0 = 7.30 \times 10^{-21}\ T^{-5.0}$	l
R244	$ClC(O)OO + SO \rightarrow Cl + SO_2 + CO_2$	1.00×10^{-11}	a
R245	$ClS + SO \rightarrow S_2O + Cl$	1.00×10^{-11}	b
R246	$S_3 + SO \rightarrow S_2O + S_2$	1.00×10^{-12}	b
R247	$S + SO + M \rightarrow S_2O + M$	$k_0 = 3.30 \times 10^{-26}\ T^{-2.0}$	b*
R248	$2SO \rightarrow SO_2 + S$	$1.00 \times 10^{-12} e^{-1700./T}$	b
R249	$2SO + M \rightarrow (SO)_2 + M$	$k_0 = 4.40 \times 10^{-31}$ $k_\infty = 1.00 \times 10^{-11}$	a
R250	$O + (SO)_2 \rightarrow S_2O + O_2$	3.00×10^{-14}	a
R251	$O + (SO)_2 \rightarrow SO + SO_2$	3.00×10^{-15}	a
R252	$S_2 + (SO)_2 \rightarrow 2S_2O$	3.30×10^{-14}	a
R253	$SO + (SO)_2 \rightarrow S_2O + SO_2$	3.30×10^{-14}	b
R254	$(SO)_2 + M \rightarrow 2SO + M$	$k_{eq}k_{eq} = 1.00 \times 10^{-28} e^{6000./T}$	a
R255	$O + SO_2 \rightarrow SO + O_2$	$8.00 \times 10^{-12} e^{-9800./T}$	a
R256	$O(^1D) + SO_2 \rightarrow SO_2 + O$	7.00×10^{-11}	b
R257	$O(^1D) + SO_2 \rightarrow SO + O_2$	1.30×10^{-10}	b
R258	$O + SO_2 + M \rightarrow SO_3 + M$	$k_0 = 1.32 \times 10^{-31} e^{-1000./T}$	k*
R259	$OH + SO_2 + M \rightarrow HSO_3 + M$	$k_0 = 1.10 \times 10^{-30}\ (T/300.)^{-4.3}$ $k_\infty = 1.60 \times 10^{-12}$	i*
R260	$HO_2 + SO_2 \rightarrow OH + SO_3$	1.00×10^{-18}	c
R261	$ClC(O)OO + SO_2 \rightarrow Cl + SO_3 + CO_2$	1.00×10^{-15}	a
R262	$O + SO_3 \rightarrow SO_2 + O_2$	$2.32 \times 10^{-16} e^{-487./T}$	b
R263	$S + SO_3 \rightarrow SO_2 + SO$	1.00×10^{-16}	b
R264	$S_2 + SO_3 \rightarrow S_2O + SO_2$	2.00×10^{-16}	b
R265	$SO + SO_3 \rightarrow 2SO_2$	2.00×10^{-15}	b

(*continued on next page*)

Table 2 (*continued*)

	Reaction	Rate constant	Reference
R266	$O + S_2O \rightarrow 2SO$	1.70×10^{-12}	a
R267	$S + S_2O \rightarrow S_2 + SO$	$1.00 \times 10^{-12}e^{-1200./T}$	b
R268	$2S_2O \rightarrow S_3 + SO_2$	1.00×10^{-14}	a
R269	$O + ClS \rightarrow SO + Cl$	1.20×10^{-10}	l
R270	$Cl + ClS \rightarrow S + Cl_2$	1.00×10^{-14}	a
R271	$Cl + ClS + M \rightarrow Cl_2S + M$	$k_0 = 1.00 \times 10^{-30}$ $k_\infty = 5.00 \times 10^{-11}$	l
R272	$S + ClS \rightarrow S_2 + Cl$	1.00×10^{-11}	l
R273	$S_2 + ClS \rightarrow S_3 + Cl$	2.00×10^{-11}	b
R274	$2ClS \rightarrow S_2 + Cl_2$	6.00×10^{-12}	l
R275	$2ClS \rightarrow Cl_2S + S$	7.50×10^{-12}	a
R276	$2ClS \rightarrow ClS_2 + Cl$	5.40×10^{-11}	l
R277	$2ClS + M \rightarrow Cl_2S_2 + M$	$k_0 = 4.00 \times 10^{-31}$ $k_\infty = 4.00 \times 10^{-12}$	a
R278	$OCS + ClS \rightarrow ClS_2 + CO$	3.00×10^{-16}	a
R279	$O + ClS_2 \rightarrow SO + ClS$	1.00×10^{-13}	b
R280	$Cl + ClS_2 \rightarrow Cl_2 + S_2$	1.00×10^{-11}	l
R281	$ClS + ClS_2 \rightarrow Cl_2S + S_2$	1.00×10^{-12}	a
R282	$H + Cl_2S \rightarrow HCl + ClS$	2.00×10^{-11}	a
R283	$Cl + Cl_2S \rightarrow Cl_2 + ClS$	1.00×10^{-19}	a
R284	$2Cl_2S \rightarrow Cl_2S_2 + Cl_2$	1.00×10^{-20}	a
R285	$Cl + Cl_2S_2 \rightarrow Cl_2 + ClS_2$	4.30×10^{-12}	a
R286	$O + OSCl \rightarrow SO_2 + Cl$	$5.00 \times 10^{-11}e^{-600./T}$	b
R287	$O + OSCl \rightarrow SO + ClO$	$2.00 \times 10^{-11}e^{-600./T}$	b
R288	$Cl + OSCl \rightarrow Cl_2 + SO$	2.30×10^{-11}	l
R289	$S + OSCl \rightarrow S_2O + Cl$	$5.00 \times 10^{-11}e^{-600./T}$	b
R290	$S + OSCl \rightarrow SO + ClS$	$2.00 \times 10^{-11}e^{-600./T}$	b
R291	$SO + OSCl \rightarrow SO_2 + ClS$	6.00×10^{-13}	l
R292	$OSCl + M \rightarrow SO + Cl + M$	$7.29 \times 10^{-21}T^{-5.0}$	a
R293	$O + ClSO_2 \rightarrow SO_2 + ClO$	1.00×10^{-11}	a
R294	$H + ClSO_2 \rightarrow SO_2 + HCl$	1.00×10^{-11}	a
R295	$Cl + ClSO_2 \rightarrow SO_2 + Cl_2$	1.00×10^{-20}	b
R296	$ClS + ClSO_2 \rightarrow SO_2 + Cl_2S$	$5.00 \times 10–12$	l
R297	$S + ClSO_2 \rightarrow SO_2 + ClS$	1.00×10^{-11}	b
R298	$S_2 + ClSO_2 \rightarrow SO_2 + ClS_2$	$5.00 \times 10^{-11}e^{-800./T}$	b
R299	$SO + ClSO_2 \rightarrow OSCl + SO_2$	$5.00 \times 10^{-11}e^{-800./T}$	b
R300	$2ClSO_2 \rightarrow Cl_2 + 2SO_2$	5.00×10^{-13}	b
R301	$O + OCS \rightarrow SO + CO$	$1.60 \times 10^{-11}e^{-2150./T}$	k
R302	$S + OCS \rightarrow S_2 + CO$	$6.63 \times 10^{-20}\ T^{2.57}e^{-1180./T}$	m
R303	$S_2 + M \rightarrow 2S + M$	$k_{eq} = 2.68 \times 10^{-25}e^{50860./T}$	f
R304	$N + O_2 \rightarrow NO + O$	$1.50 \times 10^{-11}e^{-3600./T}$	c
R305	$HNO + O_2 \rightarrow NO + HO_2$	$5.25 \times 10^{-12}e^{-1510./T}$	n
R306	$N + O_3 \rightarrow NO + O_2$	2.00×10^{-16}	c
R307	$N + OH \rightarrow NO + H$	$3.80 \times 10^{-11}e^{85./T}$	o
R308	$O_2(^1\Delta) + N \rightarrow NO + O$	9.00×10^{-17}	c
R309	$N + HO_2 \rightarrow NO + OH$	2.20×10^{-11}	p
R310	$2\ N + M \rightarrow N_2 + M$	$k_0 = 8.27 \times 10^{-34}e^{490./T}$	q
R311	$O(^1D) + N_2 + M \rightarrow N_2O + M$	$k_0 = 3.50 \times 10^{-37}\ (T/300.)^{-0.6}$	c
R312	$O + NO + M \rightarrow NO_2 + M$	$k_0 = 9.00 \times 10^{-31}\ (T/300.)^{-1.5}$ $k_\infty = 3.00 \times 10^{-11}$	c
R313	$O_3 + NO \rightarrow NO_2 + O_2$	$3.00 \times 10^{-12}e^{-1500./T}$	c
R314	$H + NO + M \rightarrow HNO + M$	$k_0 = 3.23 \times 10^{-32}$	r
R315	$OH + NO + M \rightarrow HNO_2 + M$	$k_0 = 7.00 \times 10^{-31}\ (T/300.)^{-2.6}$ $k_\infty = 3.60 \times 10^{-11}\ (T/300.)^{-0.1}$	c
R316	$HO_2 + NO \rightarrow NO_2 + OH$	$3.50 \times 10^{-12}e^{250./T}$	c
R317	$N + NO \rightarrow N_2 + O$	$2.10 \times 10^{-11}e^{100./T}$	c
R318	$O + NO_2 \rightarrow NO + O_2$	$5.60 \times 10^{-12}e^{180./T}$	c
R319	$O + NO_2 + M \rightarrow NO_3 + M$	$k_0 = 2.50 \times 10^{-31}\ (T/300.)^{-1.8}$ $k_\infty = 2.20 \times 10^{-11}(T/300.)^{-0.7}$	c
R320	$O_3 + NO_2 \rightarrow NO_3 + O_2$	$1.20 \times 10^{-13}e^{-2450./T}$	c
R321	$H + NO_2 \rightarrow OH + NO$	$4.00 \times 10^{-10}e^{340./T}$	c
R322	$OH + NO_2 + M \rightarrow HNO_3 + M$	$k_0 = 2.00 \times 10^{-30}\ (T/300.)^{-3.0}$ $k_\infty = 2.50 \times 10^{-11}e^{300./T}$	c
R323	$HO_2 + NO_2 \rightarrow HNO_2 + O_2$	5.00×10^{-16}	c
R324	$N + NO_2 \rightarrow N_2O + O$	$5.80 \times 10^{-12}e^{220./T}$	c
R325	$NO_3 + NO_2 \rightarrow NO + NO_2 + O_2$	$4.50 \times 10^{-14}e^{-1260./T}$	c
R326	$O + NO_3 \rightarrow O_2 + NO_2$	1.00×10^{-11}	c
R327	$H + NO_3 \rightarrow OH + NO_2$	1.10×10^{-10}	s
R328	$OH + NO_3 \rightarrow HO_2 + NO_2$	2.20×10^{-11}	c
R329	$HO_2 + NO_3 \rightarrow HNO_3 + O_2$	3.50×10^{-12}	c
R330	$NO + NO_3 \rightarrow 2NO_2$	$1.50 \times 10^{-11}e^{170./T}$	c
R331	$2NO_3 \rightarrow 2NO_2 + O_2$	$8.50 \times 10^{-13}e^{2450./T}$	c
R332	$HCl + NO_3 \rightarrow HNO_3 + Cl$	5.00×10^{-17}	c
R333	$CO + NO_3 \rightarrow NO_2 + CO_2$	4.00×10^{-19}	c
R334	$O(^1D) + N_2O \rightarrow 2NO$	6.70×10^{-11}	c

Table 2 (*continued*)

	Reaction	Rate constant	Reference
R335	$O(^1D) + N_2O \rightarrow N_2 + O_2$	4.90×10^{-11}	c
R336	$H + HNO \rightarrow H_2 + NO$	1.30×10^{-10}	t
R337	$OH + HNO \rightarrow H_2O + NO$	5.00×10^{-11}	u
R338	$O_3 + HNO_2 \rightarrow O_2 + HNO_3$	5.00×10^{-19}	c
R339	$OH + HNO_2 \rightarrow H_2O + NO_2$	$1.80 \times 10^{-11}e^{-390./T}$	c
R340	$O + HNO_3 \rightarrow OH + NO_3$	3.00×10^{-17}	c
R341	$OH + HNO_3 \rightarrow NO_3 + H_2O$	$7.20 \times 10^{-15}e^{785./T}$	c
R342	$Cl + NO_3 \rightarrow ClO + NO_2$	2.40×10^{-11}	c
R343	$Cl + HNO_3 \rightarrow HCl + NO_3$	2.00×10^{-16}	c
R344	$ClO + NO \rightarrow Cl + NO_2$	$6.40 \times 10^{-12}e^{290./T}$	c
R345	$ClO + N_2O \rightarrow 2NO + Cl$	$1.00 \times 10^{-12}e^{-4300./T}$	c
R346	$SO + NO_2 \rightarrow SO_2 + NO$	1.40×10^{-11}	c
R347	$SO_2 + NO_2 \rightarrow SO_3 + NO$	2.00×10^{-26}	c
R348	$SO_2 + NO_3 \rightarrow SO_3 + NO_2$	7.00×10^{-21}	c
R349	$OCS + NO_3 \rightarrow CO + SO + NO_2$	1.00×10^{-16}	k
R350	S_x + Aerosol → Aerosol	See Appendix B	

Note: *M* represents the third body such as N_2 or CO_2 for three-body reactions. Two-body rate constants and high-pressure limiting rate constants for three-body reactions (k_∞) are in units of $cm^3\ s^{-1}$. Low-pressure limiting rate constants for three-body reactions (k_0) are in units of $cm^6\ s^{-1}$. k_{eq} is the equilibrium constant such that the coefficient for the reverse reaction is calculated as $k_{eq}/k_{forward}$. The entropies and enthalpies used for the k_{eq} calculations are taken from reference (f).

References: (a) Mills (1998) and references therein; (b) Moses et al. (2002) and references therein; (c) Sander et al. (2002) and references therein; (d) Baulch et al. (1992) and references therein; (e) Yung and DeMore (1982) and references therein; (f) Chase et al. (1985) (JANAF thermochemical tables) and references therein; (g) Moses et al. (2000) and references therein; (h) Baulch et al. (1981) and references therein; (i) Sander et al. (2006) and references therein; (j) Lovejoy et al. (1996); (k) Atkinson et al. (2004) and references therein; (l) Mills et al. (2007a) and references therein; (m) Lu et al. (2006); (n) Bryukov et al. (1993); (o) Atkinson et al. (1989) and references therein; (p) Brune et al. (1983); (q) Campbell and Thrush (1967); (r) Riley et al. (2003); (s) He et al. (1993); (s) Dodonov et al. (1981); (t) Sun et al. (2001).

[*] Reaction rate coefficients corrected by factors of 3.3 and 8.2 for the higher efficiency of the third body CO_2 than N_2 (R247, R258, R259) and Ar (R240), respectively (Singleton and Cvetanovic, 1988).

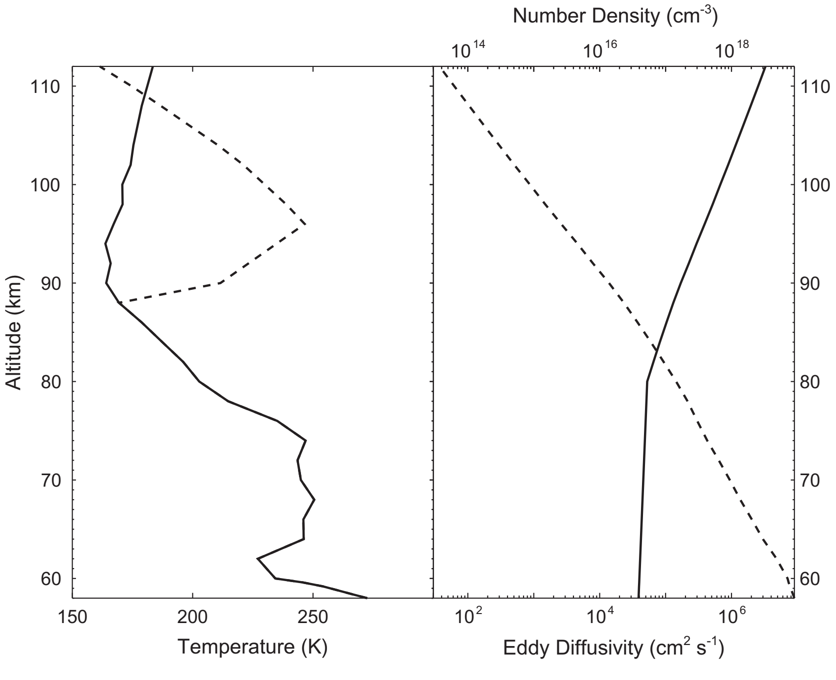

Fig. 1. Left panel: daytime temperature profile (solid) and nighttime temperature profile (dashed). Right panel: eddy diffusivity profile (solid) and total number density profile (dashed).

study: model A with enhanced H_2SO_4 abundance above 90 km and model B with enhanced S_8 abundance above 90 km. In both models we fix the vertical profiles of N_2, H_2O, and H_2SO_4. The N_2 profile is given by a constant mixing ratio of 3.5%. The H_2O profile (see Fig. 3) is prescribed on the basis of the Venus Express observations (Bertaux et al., 2007) above 70 km and is assumed to be constant below. The accommodation coefficient of the sulfur nucleation is set to unity (the upper limit) in the standard model.

The H_2SO_4 saturation vapor pressure (SVP) and the photolysis cross sections are discussed in Appendices C and D, respectively. Appendix C also shows that the H_2SO_4 weight percent profile derived from thermodynamics under the conditions of the Venus mesosphere is consistent with the photometric observations. Model A uses the nighttime H_2SO_4 vapor abundance (Fig. A6) and the H_2SO_4 photolysis cross sections with high UV cross section in the interval 195–330 nm (dashed line in Fig. A7). The H_2SO_4 abundance above 90 km is scaled to reproduce the observed SO and SO_2 data. The day and nighttime S_x saturated mixing ratio profiles based on Lyons (2008) are shown in Fig. A6. The S_8 mixing ratio under nighttime temperature could achieve ppb levels at ~96 km. Based on this, we fix the S_8 profile in model B as the sulfur source. The S_8 profile is composed of two parts: (1) below 90 km, we use the output from model A, which shows the S_8 concentration is undersaturated; (2) above 90 km, we scale the S_8 saturated vapor abundances under nighttime temperature to match the observations. We also adopt the daytime H_2SO_4 vapor abundance and the H_2SO_4 photolysis cross sections with low UV cross section in the interval 195–330 nm (solid line in Fig. A7); therefore the H_2SO_4 photolysis has almost no contribution to the sulfur enhancement in model B.

The SO_2 and OCS mixing ratios at 58 km are set to 3.5 ppm and 1.5 ppm, respectively. The upper and lower boundary conditions for the important species are listed in Table 3. We set the HCl mixing ratio as 0.4 ppm at 58 km, which is about a factor of 2 larger than the Venus Express observations (Bertaux et al., 2007). However, other observations support the 0.4 ppm HCl (Connes et al., 1967; Krasnopolsky, 2010a). We argue that since ClC(O)OO is the key species to convert CO and O_2 to CO_2 (Mills et al., 2007), 0.4 ppm HCl is needed in our model to constrain the total column abundances of O_2.

3. Model results

3.1. Enhanced H_2SO_4 case (model A)

In model A, the saturation ratio of H_2SO_4 is 0.25 (undersaturated H_2SO_4 under nighttime temperature), corresponding to the peak value ∼0.2 ppm at 96 km. Figs. 2–8 show the volume mixing ratios of oxygen, hydrogen (including HO_x), chlorine, chlorine–sulfur species, elemental sulfurs, nitrogen species, and sulfur oxides, respectively. The observations of SO, SO_2 and OCS are also plotted in Fig. 8.

The model outputs of oxygen, hydrogen and chlorine species generally agree with the previous studies (model C in Yung and DeMore (1982); the one-sigma model in Mills (1998)). The differences arise mainly from the differences of the temperature profiles and radiation field between the polar region in our model and the mid-latitude in the previous models. Compared with the temperature profile from Seiff (1983) used in the previous models, the current profile at 70°N is colder in the upper cloud layer (58–70 km) but warmer between 70 km and 80 km. The O_2 profile is consistent with the one-sigma model in Mills (1998). The concentrations of chlorine species in model A are lower than those in model C of Yung and DeMore (1982) mainly because of the lower boundary values of HCl (0.8 ppm in their model C and 0.4 ppm in our model). The abundances of chlorine-sulfur species in our model are slightly larger than those from Mills (1998) near the lower boundary because there is more OCS at the lower boundary of the model A. The profile for OCS in Fig. 8 differs significantly from that in Fig. 1 of Yung et al. (2009). Although the secondary peak around 80 km is present in both figures, it is much smaller in the present model. The main reason is that the peak is produced by S + CO, where the S atoms are ultimately derived from SO_2 photolysis. The model of Yung et al. (2009) is primarily intended to study the sulfur chemistry in the lower atmosphere, and its SO_2 concentrations above the cloud tops exceed the observational constraints. We should refer to Fig. 8 as a more realistic representation of the concentrations of sulfur species in the middle atmosphere. The nitrogen species in our model are less than that in model B of Yung and DeMore (1982) simply because their lower boundary value of NO is 30 ppb, which is about six times larger than the observed values, 5.5 ppb on average at 65 km (Krasnopolsky, 2006). Since the polysulfur chemistry has been updated based on Moses et al. (2002), model A results are different from those of Mills (1998). But the polysulfur chemistry has large uncertainties and more laboratory measurements of the reaction coefficients are needed (see discussions in Section 4). Concentrations of sulfur oxides are obviously different from those of early models when we include the sulfur source above 90 km.

Table 3
Boundary conditions.

Species	Lower boundary at 58 km	Upper boundary at 112 km
O	$v = v_m$	$\Phi = -5.03 \times 10^{11}$
O_2	$v = v_m$	$\Phi = 9.00 \times 10^{8}$
$O_2(^1\Delta)$	$v = v_m$	$\Phi = 3.00 \times 10^{8}$
Cl	$v = v_m$	$\Phi = -1.00 \times 10^{7}$
HCl	$f = 4.00 \times 10^{-7}$	$\Phi = 1.00 \times 10^{7}$
CO	$f = 4.50 \times 10^{-5}$	$\Phi = -5.03 \times 10^{11}$
CO_2	$f = 0.965$	$\Phi = 5.03 \times 10^{11}$
SO_2	$f = 3.50 \times 10^{-6}$	$\Phi = 0$
OCS	$f = 1.50 \times 10^{-6}$	$\Phi = 0$
N	$v = v_m$	$\Phi = -3.00 \times 10^{8}$
NO	$f = 5.50 \times 10^{-9}$	$\Phi = 0$
Other species	$v = v_m$	$\Phi = 0$

Note: The symbols f, Φ and v refer to the volume mixing ratio and flux ($cm^{-2}\ s^{-1}$) and velocity ($cm\ s^{-1}$), respectively. The positive sign of Φ means the upward flow. The upper boundary fluxes are from Mills (1998). $\Phi = 0$ means the photochemical equilibrium state. At the lower boundary, all other species not listed here are assumed to diffuse downward with the maximum deposition velocity (dry deposition) $v_m = K/H$, where K and H are the eddy diffusivity and scale height at 58 km, respectively. The lower boundary conditions of CO, HCl and CO_2 are from Yung and DeMore (1982) and Mills (1998). The N and NO boundary conditions are from Krasnopolsky (2006). SO_2 and OCS lower boundary mixing ratios are set to match the observations from Belyaev et al. (2012) and Krasnopolsky (2010), respectively.

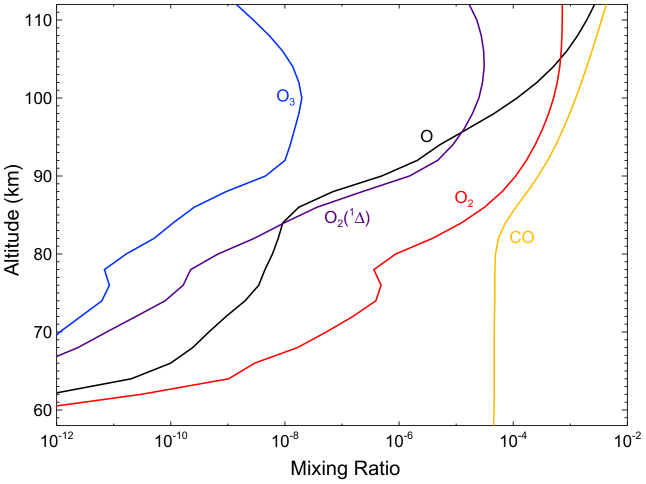

Fig. 2. Volume mixing ratio profiles of the oxygen species from model A.

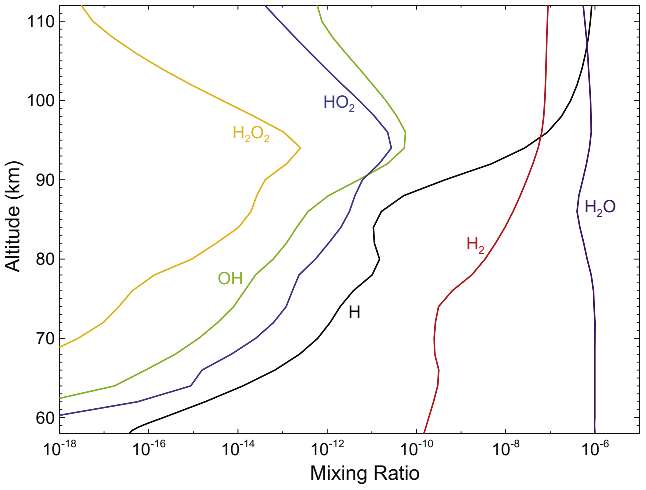

Fig. 3. Same as Fig. 2, for hydrogen species.

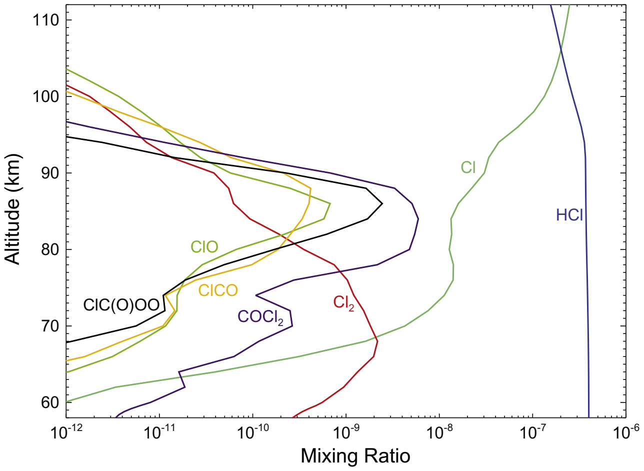

Fig. 4. Same as Fig. 2, for chlorine species.

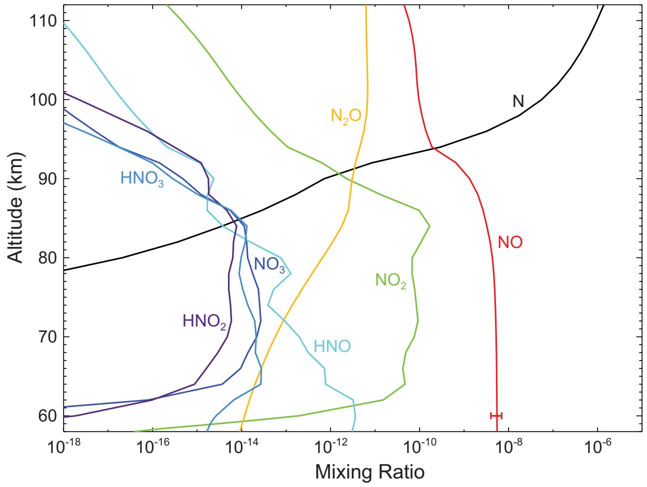

Fig. 7. Same as Fig. 2, for nitrogen species. The NO measurement (5.5 ± 1.5 ppb) is from Krasnopolsky (2006).

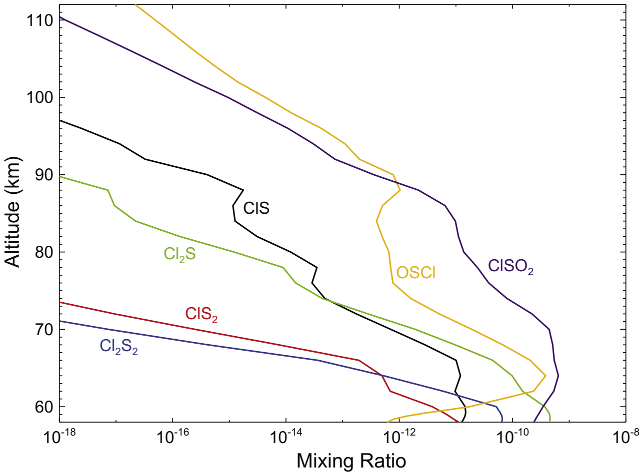

Fig. 5. Same as Fig. 2, for chlorine–sulfur species.

The photolysis of the parent species CO_2, OCS, SO_2, H_2O and HCl, which are transported by eddy diffusion from 58 km, provides the sources for the other species. Although the sulfur chemistry is closely coupled with the oxygen and chlorine chemistry in the region 60–70 km, the sulfur species have little effect on the abundances of the oxygen species (including HO_x) and chlorine species above 70 km, but not vice versa. In other words, the model without sulfur chemistry would produce roughly the same amount of oxygen and chlorine species as the model with sulfur species does above 70 km where the sulfur species are less abundant and can no longer tie up the chlorine and oxygen species. The free oxygen and chlorine bearing radicals, such as O, OH, Cl and ClO, are the key catalysts in recycling sulfur species. On the other hand, the sulfur species do not act as catalysts. Therefore, to some extent the sulfur cycle in the mesosphere can be separated from the other cycles above 70 km. Fig. 9 illustrates the important pathways of the sulfur cycle. For simplicity, the chlorosulfane chemistry and polysulfur chemistry are not shown here. See Mills and Allen (2007) and Yung et al. (2009) for detailed discussions. A fast cycle, including the photodissociation and

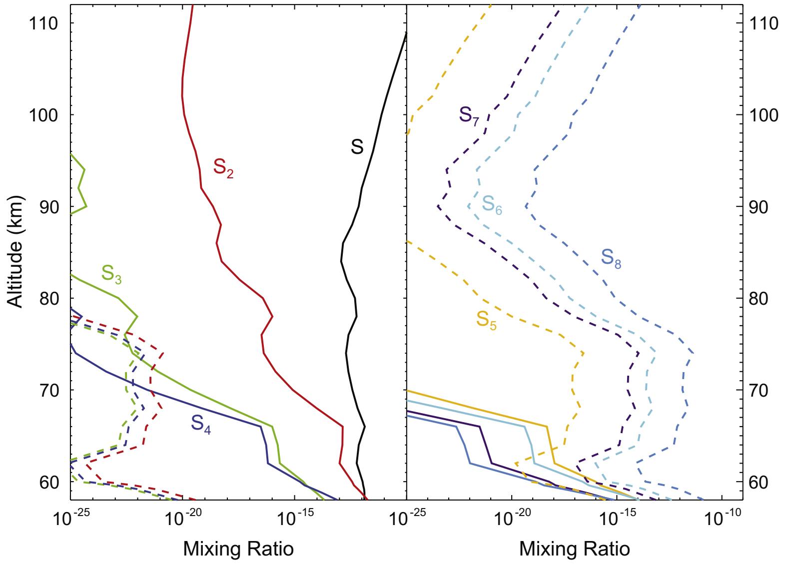

Fig. 6. Volume mixing ratio profiles (solid) of the elemental sulfur species from model A. The dashed lines are the monoclinic S_x saturated mixing ratio profiles over solid S_x based on Lyons (2008), in equilibrium with the daytime temperatures.

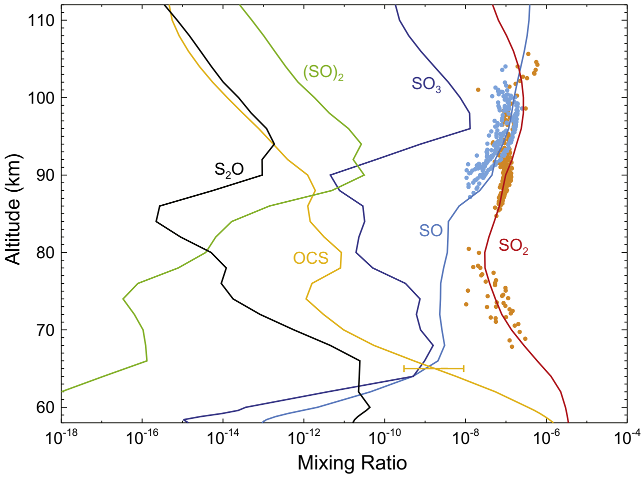

Fig. 8. Same as Fig. 2, for the sulfur oxides. The SO_2 and SO observations with errorbars are from the Belyaev et al. (2012). The temperature at 100 km is 165–170 K for the observations. The OCS measurement (0.3–9 ppb with the mean value of 3 ppb) is from Krasnopolsky (2010).

oxidization processes, exists among the sulfur species. Below 90 km, H_2SO_4 and S_x act as the ultimate sinks rather than the sources of the sulfur species in the region. The total production rate of H_2SO_4 from 58 to 112 km is 5.6×10^{11} cm^{-2} s^{-1} with a peak value of 1.3×10^{6} cm^{-3} s^{-1} around 64 km, while the total loss rate of gaseous elemental sulfur to aerosol through heterogeneous nucleation processes is 2.6×10^{12} cm^{-2} s^{-1}, when summed across all elemental sulfurs that are lost, equivalent to a sulfur atom loss rate $\sim 3.3 \times 10^{12}$ cm^{-2} s^{-1}. Therefore, the major sink of sulfur species in model A is the polysulfur aerosols. The polysulfur sink decreases with altitude mainly because both the aerosol and gaseous sulfur species are less abundant at higher altitude (Fig. 6, also see the discussion in Section 4). For reference, the Krasnopolsky and Pollack model (1994) requires the H_2SO_4 production rate of 2.2×10^{12} cm^{-2} s^{-1}. Some previous models range from 9×10^{11} to 1×10^{13} cm^{-2} s^{-1} (Yung and DeMore, 1982; Krasnopolsky and Pollack, 1994). So the H_2SO_4 production rate in model A is lower than those previously modeled values.

Below ∼65 km, $ClSO_2$ is in chemical equilibrium with SO_2. SO_2 reacts with the chlorine radical: $Cl + SO_2 + CO_2 \rightarrow ClSO_2 + CO_2$, and $ClSO_2$ reacts with O, S, S_2, SO, $ClSO_2$, etc. (Reactions R293–R300 in Table 2) to return back SO_2 and produce chlorine species including chlorosulfanes. Above ∼65 km, photolysis of SO_2 becomes the dominant sink, with a minor branch of oxidization to SO_3. The three-body reaction O + SO produces more SO_2, and ClO and ClC(O)OO reacting with SO also play important roles in SO_2 production. The major production and loss rates for SO, SO_2 and SO_3 in model A are plotted in Fig. 10.

The SO and SO_2 inversion layers above 80 km are successfully reproduced in model A (Fig. 8) although the agreement between the model results and observations is not perfect. We attribute the discrepancy to the constant H_2SO_4 saturation ratio above 90 km. The SO_2 measurements imply that the H_2SO_4 abundance in model A might be underestimated above 100 km. The chemistry is mainly driven by the photolysis and reactions with O and O_2. The fast recycling between the sulfur species can be seen from the largest production and loss rates in Fig. 10. At 96 km where the peaks of the reaction rates are, the SO_3 photolysis rate ($\sim 1.5 \times 10^{3}$ cm^{-3} s^{-1}) and $SO_3 + H_2O$ rate ($\sim 1.5 \times 10^{3}$ cm^{-3} s^{-1}) are roughly comparable, which implies about half of the sulfur in H_2SO_4 goes into SO_x and produces the inversion layers of SO_2 and SO. Model A predicts the existence of an SO_3 inversion layer, with a peak value of ∼13 ppb at 96 km. More discussion will be provided in Section 4.

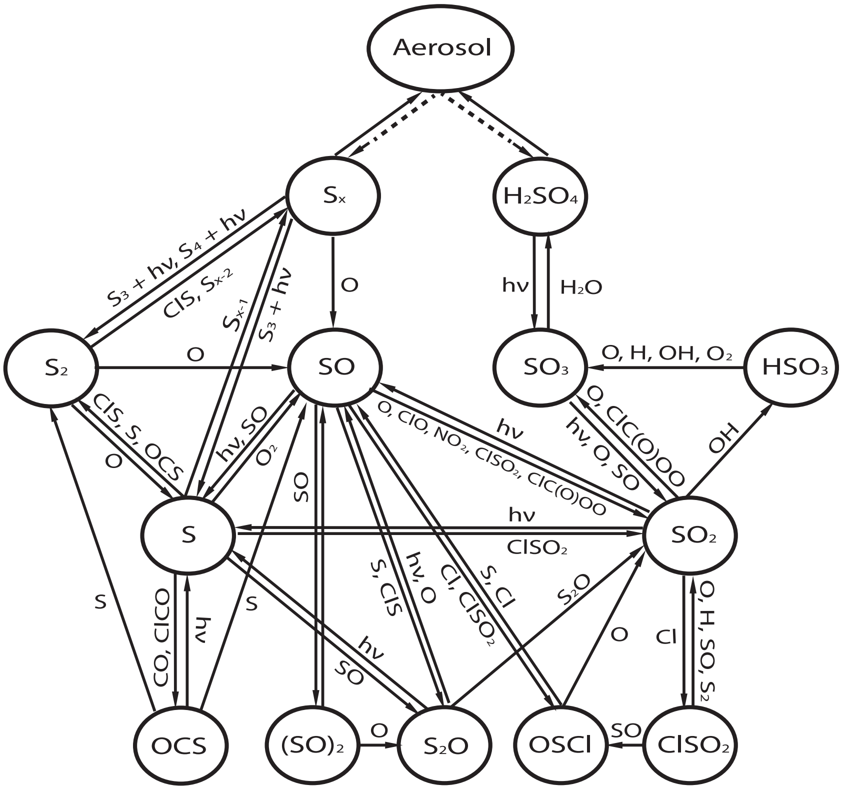

Fig. 9. Important chemical pathways for sulfur species.

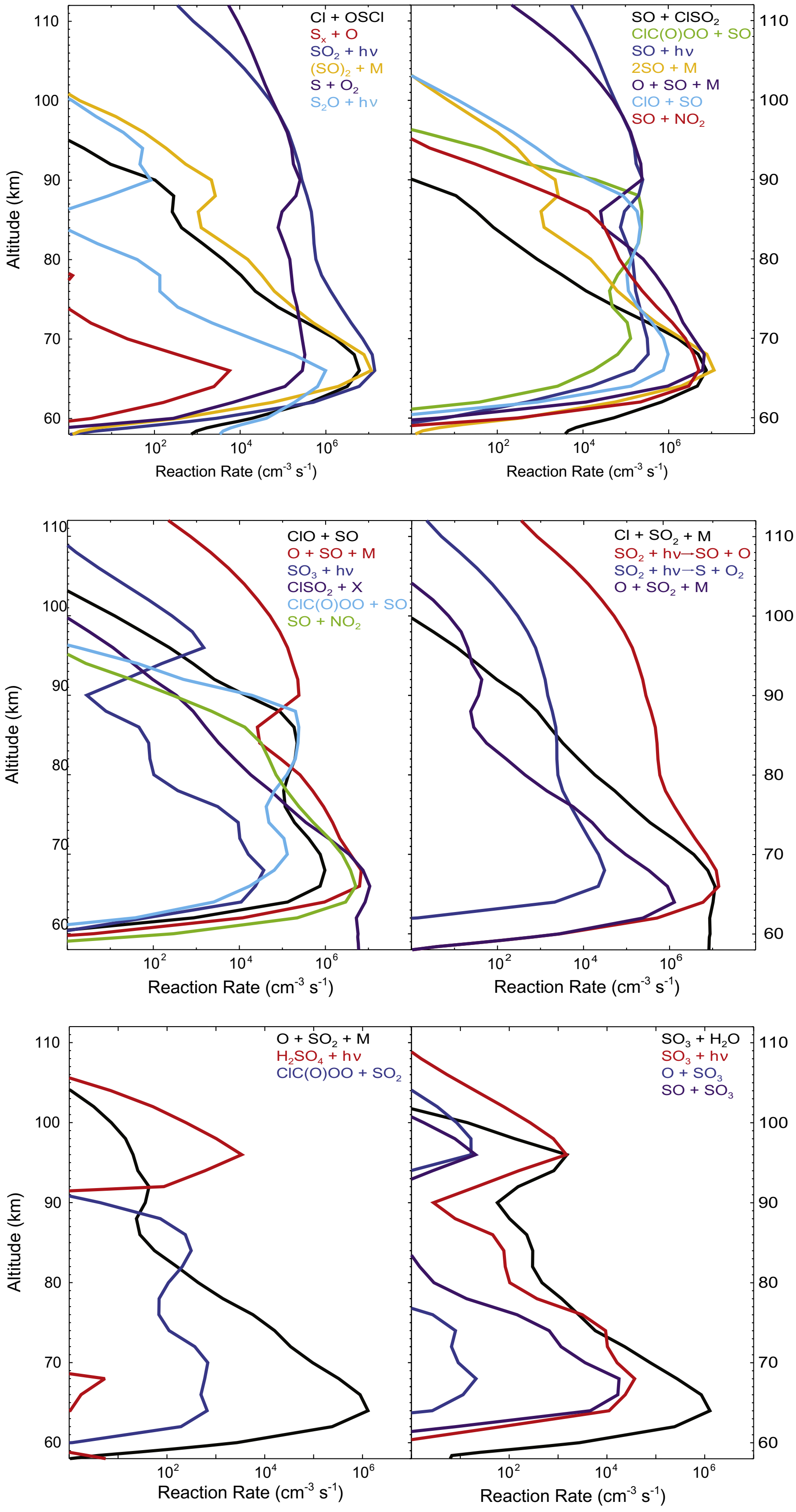

Fig. 10. Important production and loss rates for SO (upper), SO_2 (middle) and SO_3 (lower) from model A.

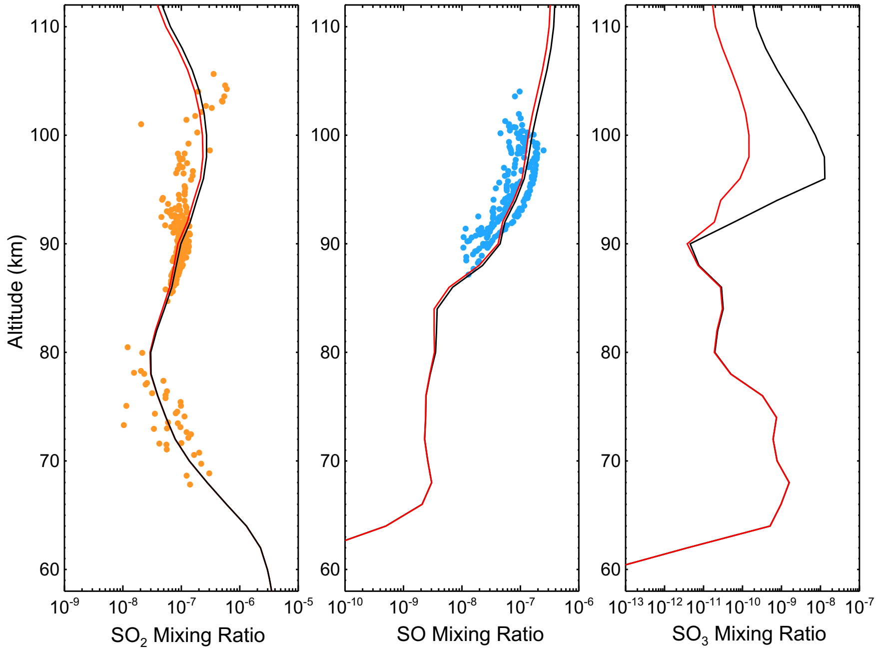

Fig. 11. Comparison of volume mixing ratio profiles of SO_2 (left), SO (middle) and SO_3 (right) from models A (black) and B (red). (For interpretation of the references to colour in this figure legend, the reader is referred to the web version of this article.)

3.2. Enhanced S_x case (model B)

The S_x aerosol might be another possible sulfur source in the upper region because S_x could react with atomic oxygen to produce SO. But this possibility is more ambiguous because: (1) The S_x aerosol has not been identified although it is the most likely UV absorber (Carlson, 2010); (2) As shown in the Fig. 6, the production of S_x is mainly confined to the region below 65 km. So the S_x in the haze layer might not be sufficient to supply the sulfur source; (3) The S_x chemistry has large uncertainty due to the lack of laboratory experiments. The reaction coefficients for S_x + O in our model were estimated by Moses et al. (2002) based on that for S_2 + O.

The required saturation ratio of S_8 is only 3×10^{-4} in order to produce the SO and SO_2 inversion layers (Fig. 11). That means we need only 0.1 ppt S_x vapor above 90 km. The SO and SO_2 profiles (and other sulfur species) from models A and B are really similar due to the fast sulfur cycle within which the major sulfur species are in quasi-equilibrium (see Section 4). However, there is a large difference in SO_3 profiles because the SO_3 in model B is derived mainly from SO_2 but not from the photolysis of H_2SO_4 in model A. The SO_3 at 96 km predicted by model B is ~0.1 ppb, which is two orders of magnitude less than that in model A. Therefore, future measurement of SO_3 could distinguish the two mechanisms.

The major production and loss rates for SO, SO_2 and SO_3 in model B are plotted in Fig. 12. Note that not only S_8 + O produces SO but other S_x derived from S_8 also react with O to produce SO, so in fact one S_8 gas molecule could eventually produce about eight SO molecules. The major differences between models A and B are the SO and SO_3 production mechanisms.

4. Discussion

4.1. Summary of chemistry above 80 km

The results of models A and B are summarized in Table 4.

For model A, the simplified SO_x chemistry from Fig. 9 can be illustrated as:

$$Aerosol \xrightleftharpoons[Condensation]{Evaporation} H_2SO_4 \underset{H_2O}{\overset{h\nu}{\rightleftharpoons}} SO_3 \underset{O}{\overset{h\nu}{\rightleftharpoons}} SO_2 \underset{O}{\overset{h\nu}{\rightleftharpoons}} SO \underset{O_2}{\overset{h\nu}{\rightleftharpoons}} S \underset{O(weak)}{\rightleftharpoons} S_x$$

Similar to model A, the chemistry in model B:

$$Aerosol \xrightleftharpoons[Condensation]{Evaporation} S_x \underset{\substack{O_2 \\ S \underset{h\nu}{\rightleftharpoons} SO}}{\overset{O}{\rightleftharpoons}} SO \underset{h\nu}{\overset{O}{\rightleftharpoons}} SO_2 \underset{h\nu}{\overset{O}{\rightleftharpoons}} SO_3 \underset{h\nu(weak)}{\overset{H_2O}{\rightleftharpoons}} H_2SO_4$$

In fact OCS, S_2O and $(SO)_2$ are also in photochemical equilibrium with the species above but not shown here (see Fig. 9). Therefore, the fast cycle allows us to derive the ratios of the sulfur species above 90 km analytically by equating the production and loss rates for each species (the subscripts refer to the reaction numbers in Tables 1 and 2):

$$\frac{[OCS]}{[S]} = \frac{k_{183}[ClCO] + k_{185}[CO][M]}{k_{302}[S] + J_{31}} \tag{1}$$

$$\frac{[S]}{[SO]} = \frac{J_{27}}{k_{166}[O_2]} \tag{2}$$

$$\frac{[S]}{[SO_2]} = \frac{J_{29}}{k_{240}[O][M]} \tag{3}$$

In model B:

$$\frac{[SO_2]}{[SO_3]} = \frac{J_{30} + k_{177}[H_2O]}{k_{258}[O][M]} \tag{4}$$

But in model A, SO_3 is approximately independent of other SO_x because of the photolysis of sulfuric acid is the principal source:

$$[SO_3] = \frac{J_{23}[H_2SO_4]}{J_{30} + k_{177}[H_2O]} \tag{5}$$

Again, SO_3 is the key species to distinguish the two pathways because other sulfur species are closely coupled to SO_2 no matter what causes the inversion layers.

The S_2O and $(SO)_2$ chemistry is less clear so it needs a more careful study in the future. In models A and B, the steady-state results are given by:

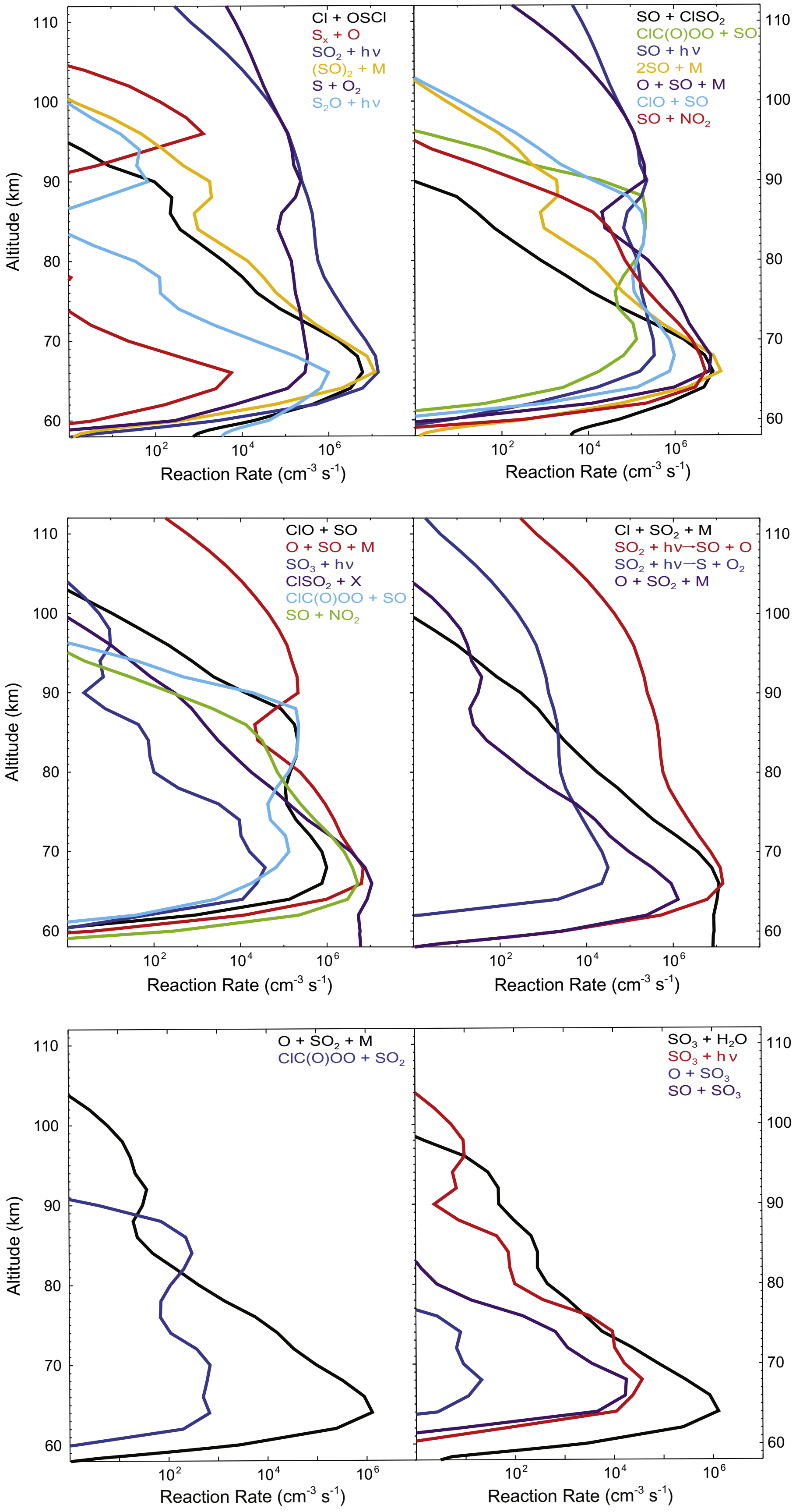

Fig. 12. Important production and loss rates of SO (upper), SO_2 (middle) and SO_3 (lower) from model B.

Table 4
Summary of the models A and B.

Parameters	Model A	Model B
H_2SO_4 vapor profile above 90 km	Fixed nightside profile (×0.25)	Fixed dayside profile
S_x vapor profile above 90 km	Free	Fixed nightside profile (×0.0003)
H_2SO_4 photolysis coefficient (s^{-1}) at 90 km	7.1×10^{-6}	7.4×10^{-8}
SO_3 column photolysis loss rate ($cm^{-2}\,s^{-1}$) above 90 km	5.8×10^{8}	8.7×10^{6}
O_2 column abundance (cm^{-2})	2.2×10^{18}	2.2×10^{18}
[a]S_x aerosol column production rate ($cm^{-2}\,s^{-1}$)	3.3×10^{12} (total)	3.3×10^{12} (total)
	1.2×10^{7} (>90 km)	1.1×10^{7} (>90 km)
H_2SO_4 column production rate ($cm^{-2}\,s^{-1}$)	5.6×10^{11} (total)	5.6×10^{11} (total)
	5.5×10^{8} (>90 km)	2.3×10^{7} (>90 km)
SO_2 column production rate ($cm^{-2}\,s^{-1}$)	2.2×10^{13} (total)	2.2×10^{13} (total)
	6.6×10^{11} (>80 km)	6.1×10^{11} (>80 km)
O column production rate ($cm^{-2}\,s^{-1}$)	1.7×10^{13} (total)	1.7×10^{13} (total)
	4.3×10^{12} (>80 km)	4.2×10^{12} (>80 km)

[a] Define the S_x aerosol production rate (converted to the sulfur content) as: $\sum_{i=1,8} i \times R(S_i)$, where $R(S_i)$ is the heterogeneous loss rates of the elemental sulfur S_i ($i = 1, 8$).

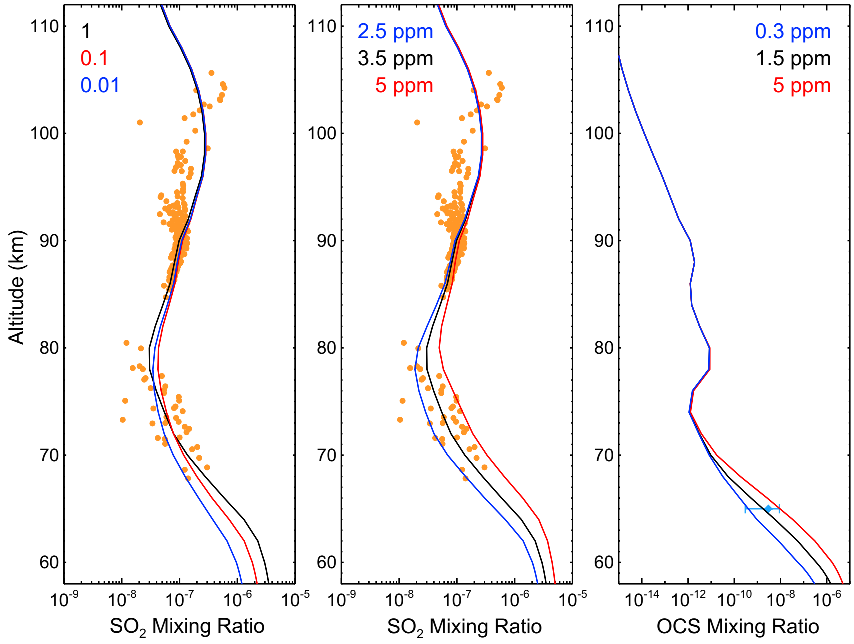

Fig. 13. Sensitivity studies based on model A. Left panel: cases for different accommodation coefficients (see labels) of the heterogeneous nucleation rate. Middle panel: cases with different boundary conditions of SO_2 (see labels). Right panel: cases with different boundary conditions of OCS (see labels).

$$\frac{[S_2O]}{[(SO)_2]} = \frac{k_{250}[O]}{J_{33} + k_{266}[O]} \tag{6}$$

$$\frac{[(SO)_2]}{[SO]} = \frac{k_{249}[SO][M]}{k_{246}[O] + k_{254}[M]} \tag{7}$$

The total column abundance of O_2 is about $\sim 2.2 \times 10^{18}$ cm^{-2} in models A and B. The atomic oxygen (O) column production rate above 80 km is $\sim 4.3 \times 10^{12}$ $cm^{-2}\,s^{-1}$. The O flux required to reproduce the mean O_2 emission of 0.52 MR in the nightside is $\sim 2.9 \times 10^{12}$ $cm^{-2}\,s^{-1}$ (Krasnopolsky, 2010c). Note that our calculation is at 70°N. If we use 45°N (mid-latitude) instead, we obtain $\sim 6 \times 10^{12}$ $cm^{-2}\,s^{-1}$. This suggests that about 50% of the O atoms produced in the dayside are transported to the nightside and recombine to form O_2. Therefore, the transport process is at least as fast as the chemical loss processes. The loss timescale of O is $\sim 10^5$–10^6 s above 80 km. The transport timescale is estimated to be $\sim 10^4$ s, based on the SSAS downward velocity ~ 43 cm s^{-1} around 100 km in the night side from Bertaux et al. (2007) and the scale height of 4 km in the lower thermosphere.

Both the SO and SO_2 profiles are derived from the observations above 90 km. They provide a test of the three-body reaction $SO + O + M \rightarrow SO_2 + M$ in the low temperature region, for which there are no laboratory measurements. The value adopted in our models is from Singleton and Cvetanovic (1988) at 298 K, $k_{240,0} = 4.2 \times 10^{-31}$ $cm^6\,s^{-1}$ and $k_{240,\infty} = 5.3 \times 10^{-11}$ $cm^3\,s^{-1}$, and has been enhanced by a factor of 8.2 for the third-body CO_2. This reaction coefficient produces the $[SO_2]/[SO] \sim 2$, which lies in the range of the Venus Express occultation observations for the terminator (Beyleav et al., 2011) and the dayside submillimeter observation range (Sandor et al., 2010). The nightside submillimeter observations find $[SO_2]/[SO] \sim 15$–50 (Sandor et al., 2010). The reaction coefficient $k_{240,0}$ derived from Venus Express observations directly is about 3×10^{-30} at 100 km (168 K). It implies that this reaction may have no or very weak temperature dependence between 160 and 300 K. Grillo et al. (1979) and Lu et al. (2003) measured the temperature dependence in the high temperature region (~300–3000 K) and the two papers provided the dependence as $T^{-1.84}$ and $T^{-2.17}$, respectively. However, this temperature dependence is too steep for the low temperature region.

One puzzle from the observed $[SO_2]/[SO]$ ratio is that the ratio seems to increase with temperature at 100 km (Belyaev, et al., 2012), although this difference is within the uncertainty associated with fewer measurements in the high temperature region (the *T*2 (180–185 K) and *T*3 (190–192 K) regions). In addition, there is difficulty in separating the SO signal from the SO_2 signal in the spectrum.

4.2. Sensitivity study

Due to the uncertainty in the adopted value of the accommodation coefficient, we test the sensitivity of model A by slowing down the heterogeneous nucleation processes (reducing α). As α decreases, the formation of S_x aerosols is slower so there are more sulfur species in the gas phase. Therefore, the model requires less SO_2 at the lower boundary to reproduce the SO_2 observations. The left panel of Fig. 13 summarizes the cases with 1× (model A), 0.1× and 0.01× α. All three cases show that the major sink of sulfur species is the polysulfur aerosol. As the polysulfur nucleation process slows down, the H_2SO_4 production rate also decreases because of the lower SO_2 abundances around 62–64 km where the H_2SO_4 production peak is. One interesting phenomenon is that, when the nucleation process is slower, the production rate of condensed S_x aerosol is less but the equivalent sulfur atom loss rate increases. This is because more high-order polysulfur molecules are produced and condense rapidly to form aerosols. Therefore, it is the result of the competition between the cycling of polysulfur and the nucleation processes. The region above 85 km is almost unaffected because the polysulfur sink at those levels is negligible. Preliminary work by Marcq et al. (2011b) suggests a correlation between cloud formation during brightening events, SO_2 depletion and enhancement in UV absorber. A possible interpretation is the conversion of SO_2 to polysulfur aerosols in the cloud region, provided that the unknown UV absorber contains polysulfur. Further work especially regarding H_2O variations is required to discriminate between this hypothesis and other possibilities.

The middle and right panels of Fig. 13 show the sensitivity to different lower boundary values of SO_2 (2.5–5 ppm) and OCS (0.3–5 ppm). These cases all lie in the observational error bars. The change of SO_2 boundary conditions mainly impacts the region below 85 km. The OCS boundary conditions affect only the upper cloud region.

The major uncertainties of model A arise from the vapor abundances and the photolysis coefficient of H_2SO_4. Since half of the sulfur in H_2SO_4 goes into SO_x, we would expect a linear relationship between $[SO_2]$ and the product of J_{32} and $[H_2SO_4]$. In model A, the J_{32} and $[H_2SO_4]$ at 96 km are $6.7 \times 10^{-6}\ s^{-1}$ and $5.0 \times 10^{8}\ cm^{-3}$, respectively, so $J_{32}[H_2SO_4]$ is $\sim 3.3 \times 10^{3}\ cm^{-3}\ s^{-1}$. For model B, although the relationship between the S_8 and SO_2 abundances is not derived explicitly, we also expect a linear relationship between the two species because all the major sulfur oxides in model B above 90 km are linearly dependent with each other. The reaction coefficients of $S_8 + O$ (k_{233}) and $[S_8]$ at 96 km are $7.0 \times 10^{-12}\ cm^3\ s^{-1}$ and $7.1 \times 10^{2}\ cm^{-3}$ respectively, so $k_{233}[S_8]$ (the product of k_{233} and $[S_8]$) is $\sim 5.0 \times 10^{-9}\ s^{-1}$. Assuming that all eight sulfur atoms in S_8 eventually go into SO, the production rate is $\sim 2 \times 10^{3}\ cm^{-3}\ s^{-1}$ given that the O abundance is $\sim 4 \times 10^{10}\ cm^{-3}$ at 96 km. This value is of the same order of magnitude as $J_{32}[H_2SO_4]$ from model A. Therefore, both models require a sulfur source at least this large to match the observations.

4.3. Sulfur budget above 90 km

The recycling of aerosols from the region below 90 km is essential to maintain the inversion in steady state because sulfur will diffuse downward due to the inverted mixing ratio gradient. The production rates of H_2SO_4 and S_x aerosol for models A and B are shown in Fig. 14. The H_2SO_4 production rate in model A has a secondary peak at 96 km where the SO_3 peak is located. But the S_x aerosol production rate above 90 km is small because the nucleation process is really slow when there are few aerosol particles to serve as condensation nuclei.

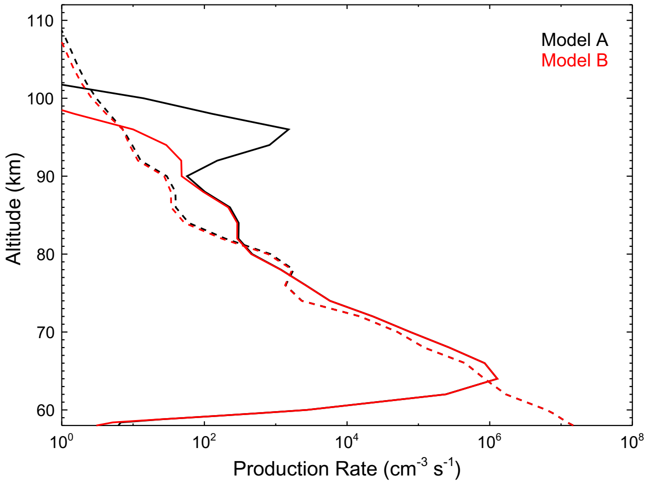

Fig. 14. Production rate profiles of H_2SO_4 (solid) and S_x (dashed) for models A (black) and B (red). (For interpretation of the references to colour in this figure legend, the reader is referred to the web version of this article.)

In model A, the net column loss rate of H_2SO_4 vapor above 90 km is $\sim 6 \times 10^{8}\ cm^{-2}\ s^{-1}$, corresponding to ∼50% of the column photolysis rate of H_2SO_4 in that region. Only ∼2% sulfur is converted into polysulfur aerosol. So the total downward sulfur flux is $\sim 6 \times 10^{8}\ cm^{-2}\ s^{-1}$ to maintain a steady state above 80 km. For reference, the $6 \times 10^{8}\ cm^{-2}\ s^{-1}$ H_2SO_4 loss rate above the region below 90 km is roughly equal the H_2SO_4 column production rate in the region of 78–90 km through the hydration of SO_3. However, it is difficult to transport the H_2SO_4 vapor upward from below 90 km to compensate the loss above because the vapors will quickly condense into the aerosols. Instead, the aerosols must be transported upward on the dayside by the SSAS circulation. Assuming that all the aerosols above 90 km are the mode 1 aerosols with mean radius 0.2 μm and density $2\ g\ cm^{-3}$, the aerosol column loss rate is $\sim 1\ cm^{-2}\ s^{-1}$. The column abundance of mode 1 aerosol above 90 km from Wilquet et al. (2009) is $\sim 5.0 \times 10^{6}\ cm^{-2}$. Therefore the aerosol lifetime is ∼100 Earth days in model A. The loss rate implies that the upward aerosol flux is also $\sim 1\ cm^{-2}\ s^{-1}$ across 90 km to supply the aerosol budget. Provided that the concentration of mode 1 aerosol at 90 km is $\sim 10\ cm^{-3}$ (Wilquet et al., 2009), the estimated flux is equivalent to an effective upward transport velocity $\sim 0.1\ cm\ s^{-1}$.

In model B, the total equivalent sulfur column loss rate of the S_x vapor above 90 km is $\sim 4 \times 10^{8}\ cm^{-2}\ s^{-1}$, which is roughly the same magnitude as the net sulfur flux from H_2SO_4 photolysis in model A, but the production rate of S_x aerosol is only $\sim 1 \times 10^{7}\ cm^{-2}\ s^{-1}$. The H_2SO_4 aerosol production rate in model B is $\sim 2 \times 10^{7}\ cm^{-2}\ s^{-1}$. Therefore, most of the sulfur from S_x aerosol diffuses downward as SO_2 and SO. For reference, the equivalent sulfur column production rate of the S_x aerosol in the region of 78–90 km is $\sim 4.0 \times 10^{8}\ cm^{-2}\ s^{-1}$. Therefore, if those aerosols can be transported upward, it would be enough to compensate for the loss in the region above 90 km. Assuming that all the polysulfur aerosol above 90 km has a mean radius of ∼0.1 μm (half of the H_2SO_4 aerosol) and the density is $2\ g\ cm^{-3}$, the aerosol column loss rate is $\sim 3\ cm^{-2}\ s^{-1}$. If the polysulfur aerosol abundance is about 1% of that of H_2SO_4 aerosol, S_x aerosol above 90 km will be removed in ∼1 Earth day. The estimated upward flux cross the 90 km level is equivalent to an effective upward transport velocity $\sim 30\ cm\ s^{-1}$.

If the SSAS circulation dominates the upper atmosphere, it might be very efficient for transporting the aerosols upward. The downward velocity at 100 km near the anti-solar point is estimated to be ~43 cm s^{-1} from the observed nighttime temperature profiles in Bertaux et al. (2007). Another derivation in Liang and Yung (2009) obtained a different value of ~1 cm s^{-1} at 100 km, which should be corrected to ~10 cm s^{-1}. So the two different calculations are consistent. However, one should always keep in mind that the SSAS circulation is a longitudinal pattern, therefore the vertical velocity should strongly depend on the solar zenith angle. The SSAS pattern from recent VTGCM model results by Bougher et al. (personal communication) show that the vertical velocity in the dayside is on the order of 10 cm s^{-1} above 100 km and on the order of 1 cm s^{-1} from 80 to 100 km. Therefore the velocity required in model A (~0.1 cm s^{-1}) is readily achieved. But the velocity implied by model B (~30 cm s^{-1}) appears to be larger than the dynamic model results.

4.4. Timescales

The dynamics in the 1-D photochemistry-diffusion model is only a simple parameterization for the complicated transition zone between 90 and 100 km. The aerosol microphysics is also simplified because we just assume the instantaneous condensations of H_2O and H_2SO_4 and ignore the aerosol growth and loss processes. Future 2-D models including SSAS, zonal wind transport, microphysical processes and photochemical processes for both the dayside and nightside hemisphere might be sufficient to represent all the dynamical and chemical processes in the upper regions. We estimate some typical timescales here.

(1) *Transport*: The timescale for the SSAS transport τ_{SSAS} is ~10^4 s (based on Bertaux et al. (2007)) for vertical transport over the 4 km scale height near 100 km. Zonal transport timescale due to Retrograde Zonal (RZ) flow τ_{RZ} is ~10^5 s for transport from the subsolar point to the antisolar point, provided that the thermal wind velocity is ~50 m s^{-1} by Piccialli et al. (2008) based on the cyclostrophic approximation. Eddy diffusion timescale τ_{eddy} is also ~10^5 s near 100 km (Fig. 15).

(2) *Aerosol condensation*: We assume that the condensation is dominated by the heterogeneous nucleation with timescale $\tau_{cond} \sim 10^4$–10^5 s (Fig. 15) for the accommodation coefficient $\alpha = 1$. τ_{cond} is inversely proportional to α in the free molecular regime for the upper region. Therefore, the lower value of α might be more appropriate for the H_2SO_4 condensation in model A since the mechanism assumes that the nighttime H_2SO_4 vapor could be transported to the dayside and undergo photolysis. Homogeneous nucleation may be important in the dayside since both of H_2SO_4 and S_x are highly supersaturated. For example, the dayside saturation ratios at 100 km are about 10^6 and 10^4 for H_2SO_4 in model A and S_8 in model B, respectively. In model A, these dayside condensation processes will compete with the photodissociation of H_2SO_4. However, the homogeneous nucleation rate markedly depends on the SVP, which is a steep function of temperature but not well determined in the lower temperature range. Due to the condensation and photolysis of H_2SO_4 in the dayside, a zonal gradient of the H_2SO_4 vapor abundance from the nightside to the dayside would be expected.

(3) *Chemistry*: H_2SO_4 photolysis timescale τ_{photo} depends on the cross section. For model A, τ_{photo} is ~10^5 s. S_x + O timescale τ_{S_x+O} depends on the reaction coefficient and the atomic oxygen abundance, τ_{S_x+O} is ~1–10 s in the model B. That is why ~0.1–1 ppt S_x could provide a sulfur source as large as the photolysis of ~0.1 ppm H_2SO_4 does. The reaction between polysulfur and atomic oxygen is so fast that it has to happen in the nightside. However, as shown above, whether the circulation could support the S_x aerosol upward flux across 90 km needs more future studies.

4.5. Basic differences between models A and B

Here, we present several basic differences between models A and B for future considerations.

First, the two mechanisms are probably applied to different horizontal regions. By roughly estimating the chemical timescales and dynamical timescales, we found that the S_x + O reaction in model B is much faster than the transport. As the S_x aerosols are evaporated in the nightside, the S_x vapor will be oxidized in less than 10 s, therefore the SO_x is first produced in the nightside and then transported to the dayside by the zonal wind and photodissociated. On the other hand, H_2SO_4 photolysis has to happen in the dayside in model A. So the SO_x should be first produced in the dayside and then transported to the nightside. A big issue of model A is the H_2SO_4 condensation rate in the dayside since it is highly supersaturated. If the homogeneous nucleation were very fast, the supersaturated vapor pressure could not be maintained, and the production of SO_2 from the photolysis of H_2SO_4 would be too small. Therefore, the nightside H_2SO_4 abundances would be also supersaturated in order to supply enough H_2SO_4 for the dayside.

Secondly, the two mechanisms might require different aerosol flux from below. Since the aerosols cannot be fully recycled above 90 km due to diffusion loss of sulfur, an upward aerosol flux is needed. The estimated aerosol flux is ~1 cm^{-2} s^{-1} and ~3 cm^{-2} s^{-1}, corresponding to an effective upward transport velocity ~0.1 cm s^{-1} and ~30 cm s^{-1} for model A and model B, respectively. However, the estimation of S_x transport velocity here is based on the assumption of the S_x/H_2SO_4 ratio ~1% (Carlson, 2010), which remains to be confirmed by future measurements.

Thirdly, in terms of possible observational evidence, model A requires H_2SO_4 number density ~10^8 cm^{-3} around 96 km in the dayside, which might be observed. The estimated abundance of S_8 in the nightside is only ~10^2 cm^{-3} around 96 km, which would be hard to observe. SO_3 might provide another possibility to distinguish the two mechanisms because SO_3 is controlled mainly by the H_2SO_4 photolysis in model A but by the SO_2 oxidization in model B. The abundance of SO_3 at 96 km is ~3.3×10^7 cm^{-3} and ~2.2×10^5 cm^{-3} for models A and B, respectively. Future observations might be able to detect this difference. On the other hand, if the SO radical is produced mainly by the polysulfur oxidization in the nightside, it might be possible to observe the nightglow of SO excited states, in analogous to the O_2 nightglow. The electronic transition of the SO ($a^1\Delta \rightarrow X^3\Sigma^-$) at 1.7 μm has been detected in Io's atmosphere (de Pater et al., 2002).

4.6. OCS above the cloud tops

The OCS mixing ratio in the upper cloud layer is puzzling. OCS originates from the lower atmosphere. Marcq et al. (2005, 2006) reported an OCS mixing ratio ~0.55 ± 0.15 ppm at ~36 km, decreasing with altitude with a gradient of −0.28 ppm/km based on the ground-based telescope IRTF observation. The VIRTIS measurement (Marcq et al., 2008) found the OCS mixing ratio ranging between 2.5 ± 1 and 4 ± 1 ppm at 33 km, agreeing with the previous value ~4.4 ppm from Pollack et al. (1993). Therefore, OCS would only be ~0.1 ppm or less in the lower cloud layer (~47 km). However, a sensitivity study of model A (Fig. 13) shows that 0.3–5 ppm OCS at the upper cloud deck (~58 km) is required to reproduce the OCS mixing ratio at 65 km in the observed range 0.3–9 ppb reported by Krasnopolsky (2010b). Krasnopolsky (2008) reported even larger values, ~14 ppb around 65 km and ~2 ppb around 70 km. Venus Express results suggest that the upper limit of OCS is 1.6 ± 2 ppb in the region 70–90 km (Vandaele et al., 2008). But model A can produce only several tens of ppt OCS around 70 km. One tentative detection of OCS reported from ground-based observations near 12 μm (Sonnabend et al., 2005) found an abundance consistent with that calculated by Mills (1998), which specified 0.1 ppm OCS at 58 km. Besides, the scale height of OCS in model A is ~1 km at 65 km, which matches only the lower limit of the observations (1–4 km from Krasnopolsky (2010b)). It seems that the eddy transport required in the upper cloud region needs to be more efficient to transport OCS upward. This is also consistent with the ~4 km scale height of SO_2 around 68 km in the Venus Express measurements. Although the eddy diffusivity at ~60 km has been estimated to be less than $4.0 \times 10^4\ \mathrm{cm^2\ s^{-1}}$ (Woo and Ishimaru, 1981), it could have large variations in the cloud layer, leading to large variation in the detected OCS values and maybe related to the decadal variation of SO_2 at the upper cloud top (see Fig. 7 of Belyaev et al. (2008)).

The unexpected large amount of OCS will affect the polysulfur production. There are two pathways to produce atomic sulfur (see Fig. 9). One is the photodissociation of SO and ClS (Mills and Allen, 2007). The other way is from the photolysis of OCS. If the OCS abundance is large (e.g. model A), the primary source of atomic sulfur below ~62 km is from the photolysis of OCS instead of that of SO and ClS. There are also two pathways to produce S_2. One is from the chlorosulfane chemistry (Mills and Allen, 2007) and the other is from the reaction between S and OCS. It turns out that the reaction rate of S + OCS in model A is as large as the ClS_2 photolysis below 60 km. Therefore if there is an abundant OCS layer near the lower boundary, it may greatly enhance the production of S_x in the 58–60 km region.

4.7. Elemental sulfur supersaturation

Even using the highest nucleation rate ($\alpha = 1$), the model A results show that the S_2, S_3, S_4 and S_5 are highly supersaturated based on the SVP from Lyons (2008) (see Fig. 6). The column abundances of gaseous S_2, S_3, S_4 and S_5 above 58 km are $1.4 \times 10^{13}\ \mathrm{cm^{-2}}$, $9.0 \times 10^{10}\ \mathrm{cm^{-2}}$, and $2.1 \times 10^{11}\ \mathrm{cm^{-2}}$, $4.3 \times 10^{9}\ \mathrm{cm^{-2}}$, respectively. S_5 is supersaturated with the saturation ratio ~1000 peaking at 60 km but decreases rapidly. The saturation ratio of S_4 is about 10^7 at the lower boundary and becomes moderately supersaturated above 76 km. S_3 is oversaturated by a factor of 10^5–10^{10} from 58 to 100 km. S_2 is extremely supersaturated at all altitudes. The saturation ratio is 10^8 at the bottom and the top, with a peak of 10^{15} at 90 km, where the heterogeneous nucleation of S_2 is negligible compared with the production processes from atomic sulfur through the three-body reaction 2S + M, and the major loss processes of S_2 are oxidization to SO and the photo-dissociation to atomic sulfur. As illustrated in Fig. 9, the main production processes of S_x can be summarized as $S + S_{x-1} \rightarrow S_x$ and $S_2 + S_{x-2} \rightarrow S_x$, but the reactions $ClS + S_2$ and $S_2O + S_2O$ are also important for S_3 production at the bottom and top of the model atmosphere, respectively. The loss mechanisms of S_x include the heterogeneous nucleation, conversion to other allotropes, and oxidization through $S_x + O \rightarrow S_{x-1} + SO$. Fig. 15 shows the comparison of the diurnally averaged photolysis timescales of S_2, S_3 and S_4 with the timescales of the nucleation and eddy transport. The S_2 loss process is dominated by the nucleation from 58 km to about 72 km where the photolysis is as fast as the nucleation, but the conversion from S_2 to S_4 is also important around 60 km. The photolysis timescales of S_3 and S_4 are of the order of 1 s, much smaller than the nucleation timescale (~10 s at 60 km and ~100 s at 70 km). Therefore, for S_3 and S_4, photolysis by visible light is the major loss pathway and the heterogeneous nucleation processes are negligible. Since the S_3 and S_4 aerosols are the possible candidates of the unknown UV absorbers although they are unstable (Carlson, 2010), the condensed S_3 and S_4 are probably produced from the heterogeneous S_x chemistry over the H_2SO_4 droplet surfaces (Lyons, 2008). Since the supersaturation ratios are very large for S_x vapors, the homogeneous nucleation process will be important and thus should be considered in future work. A proper treatment of the microphysical processes coupled with atmosphere dynamical processes within the cloud layer is needed to elucidate the S_x chemistry.

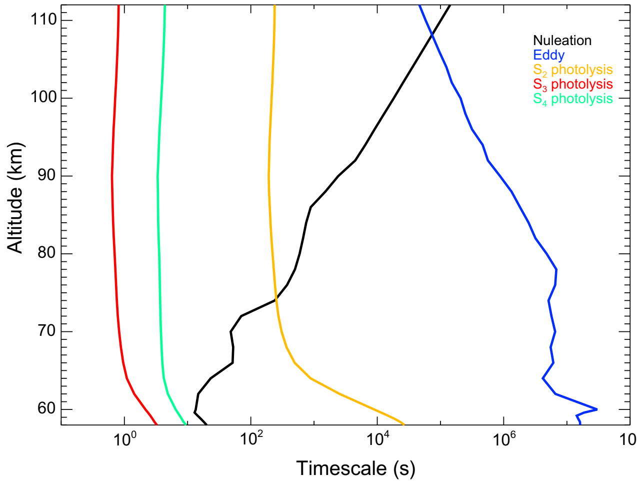

Fig. 15. Timescales for the heterogeneous nucleation, eddy transport and photolysis for S_2, S_3 and S_4.

4.8. Alternative hypotheses

Eddy diffusion is able to transport the species only from a region of high mixing ratio to that of a low mixing ratio, and so it cannot generate an inversion layer. A sudden large injection of SO_2 from either volcano (Smrekar et al., 2010) or the instability in the cloud region (e.g., VMC measurements from Markiewicz et al. (2007)) may provide a sulfur source at ~70 km, where the long-term natural variability of SO_2 has been documented but not understood. However, it is difficult for these mechanisms to explain the SO_2 inversion layer above 80 km because: (1) Volcano eruption could only reach 70 km but not higher based on a recent Venus convective plume model (Glaze et al., 2010); (2) Even if the sudden injection reaches ~100 km high, it is also difficult to maintain the steady SO_2 inversion for an extended period in the Venus Express era because the gas-phase SO_2 lifetime is short (~a few Earth days or less above 70 km). A continuous upwelling of SO_2 from the lower region to the upper region (advection) is possible although the dynamics maintaining the inversion profiles is not understood. The upward flux can be estimated by balancing the downward flux by diffusion:

$$\Phi = K_{zz}[M]\frac{df}{dz} \tag{8}$$

where Φ is the vertical flux, K_{zz} eddy diffusivity, $[M]$ number density, f mixing ratio, and z altitude. Assuming the $K_{zz} \sim 10^6\ \mathrm{cm^2\ s^{-1}}$, $df \sim 10^{-7}$, $[M] \sim 10^{17}\ \mathrm{cm^{-3}}$ (at 80 km), $dz \sim 10$ km (80–90 km), we obtain $\Phi \sim 10^{10}\ \mathrm{cm^{-2}\ s^{-1}}$. To maintain the inversion requires an equal upward flux at 80 km.

Compared with the dynamical mechanism which transports SO_2 directly from 80 km, our mechanism of in situ chemical production from parents transported in aerosol is more plausible because: (1) the inversion can be explained by the shape of the equilibrium vapor pressure profile above 90 km (models A and B); (2) it needs the upward transport of aerosols only around the 90 km region, where the SSAS circulation is strong and has been verified by the nighttime warm layer (Bertaux et al., 2007).

5. Summary and conclusion

This study is motivated by the recent measurements from Venus Express, especially the SO_2 profile from 70 to 110 km and the SO profile above 80 km, and some ground-based observations (SO and SO_2 from Sandor et al. (2010); OCS from Krasnopolsky (2010b)). The three primary chemical cycles: oxygen cycle, chlorine cycle and sulfur cycle are closely coupled in the upper cloud region. We included the heterogeneous nucleation of elemental sulfur and found that the S_2, S_3, S_4 and S_5 near the lower boundary (58 km) are highly supersaturated, even using the fastest removal rates by nucleation. Mills and Allen (2007) pointed out that the chlorosulfanes chemistry may play an important role in producing the polysulfurs in the upper cloud layer. However, in order to reproduce the recent ground-based observations, the required OCS mixing ratio at the lower boundary (1.5 ppm) is found to be significantly larger than the previous estimations (e.g. Yung et al., 2009). This enhanced OCS layer near the lower boundary would greatly increase the polysulfur production rate through the photolysis to atomic sulfur. But it is also possible to reduce the required OCS abundance at the lower boundary if we increase the eddy diffusion transport in the upper cloud layer.

In the region above 80 km, we propose two possible solutions to explain the inversion layer of SO_2. The essence of our idea to solve this problem is to 'reverse' the sulfur cycle in the region below 80 km. In 58–80 km, the SO_2 and OCS are the parent species transported from the lower atmosphere as the sulfur sources, while the H_2SO_4 and possible polysulfur aerosols are considered to be the ultimate sulfur sinks and their production rates are shown in Fig. 14. However, in the upper region the aerosols might become the sulfur source rather than the sink to provide enough sulfur for the inversion layers but it requires large aerosol evaporation. We relate this possible evaporation to the warm layer above 90 km in the night side observed by Venus Express (Bertaux et al., 2007). Therefore the SO and SO_2 inversion layers above 90 km are the natural results of the temperature inversion induced by the adiabatic heating of the SSAS flow. While the inversion layers in the region between 80 and 90 km are due to the downward diffusion from the lower thermosphere.

If H_2SO_4 aerosol is the source, the cross section of H_2SO_4 photolysis and the SVP is needed to be determined accurately. However, the laboratory work has yet to be done. From the modeling results, the possible solutions are:

(1) Use the photolysis cross sections from Lane and Kjaergaard (2008) for the UV region and Mills et al. (2005) and Feierabend et al. (2006) data for the visible region, but the H_2SO_4 saturation ratio is about $\sim$100 under nighttime temperature. That means the large supersaturation exists not only in the dayside but also in the nightside. The photolysis coefficient (J_{32}) at 90 km is $\sim 7.3 \times 10^{-8}$ s^{-1}.
(2) Use the UV cross sections from Lane and Kjaergaard (2008) and $H_2SO_4{\cdot}H_2O$ cross sections in the visible region from Vaida et al. (2003). This case requires that the hydrate abundance be roughly the same order of magnitude of the pure H_2SO_4 saturated vapor abundance with the saturation ratio $\sim$0.25 under nighttime temperature. The photolysis coefficient at 90 km is $\sim 6.8 \times 10^{-6}$ s^{-1}.
(3) Use the same cross sections as (1) but also use 1×10^{-21} cm^2 molecule^{-1} in the UV region of 195–330 nm, as shown by the dashed line in Fig. A7. The required H_2SO_4 saturation ratio is $\sim$0.25 under nighttime temperature. The photolysis coefficient at 90 km is $\sim 7.0 \times 10^{-6}$ s^{-1}.

The major difference between (3) and the other two possibilities (see Zhang et al., 2010) is that, in (3) the photolysis rate is contributed mainly by the UV flux, while in (1) and (2) the dominant sources are the visible and IR photons.

In model A we discussed possibility (3), and the model B considers the S_x aerosol as the source instead. The models A and B show some similar behaviors, which represent the general features of the upper region chemistry despite the different sulfur sources. Although there are uncertainties of the model parameters, the calculated SO_2 mixing ratio merely depends on the input sulfur flux: in terms of the H_2SO_4 photolysis production rate in model A and the S_8 oxidization rate in model B, respectively. Because of the existence of the fast sulfur cycle, we consider all the sulfur oxides in the upper region as a box. The sulfur flux flow in the upper atmosphere is summarized in Fig. 16 to illustrate the vertical transport and gas–particle conversion processes. The required sulfur flux inputs in the box above 90 km is $\sim 6 \times 10^8$ cm^{-2} s^{-1}, roughly consistent in both models A and B. All the sulfur oxides output from models A and B, except SO_3, are very similar. This is because that the gas phase sulfur chemistry in the upper region is simpler than that in the lower region (below 80 km) because it is driven by the photolysis reactions and backward recombination with O and O_2. However, the complexity comes from the coupling of the gaseous chemistry with the aerosol microphysics and the SSAS and zonal transport, both of which are poorly determined at this time. Thus, the calculations cannot be considered a proof of our hypothesis, but a demonstration of its plausibility. Future observations and more complete modeling work are needed to fully reveal the behavior of the coupled system.

Finally, we briefly summarize the following important tasks for the future.

Observations:

(1) Abundances of SO_3 and H_2SO_4 in the lower thermosphere and SO nightglow in the nightside and better constraints of SO_2 and OCS abundances in the upper cloud region. During the review process of this current paper, Sandor et al. (2012) reported their observations on the sulfuric acid in Venus' 85–100 km upper mesosphere. The upper limit of

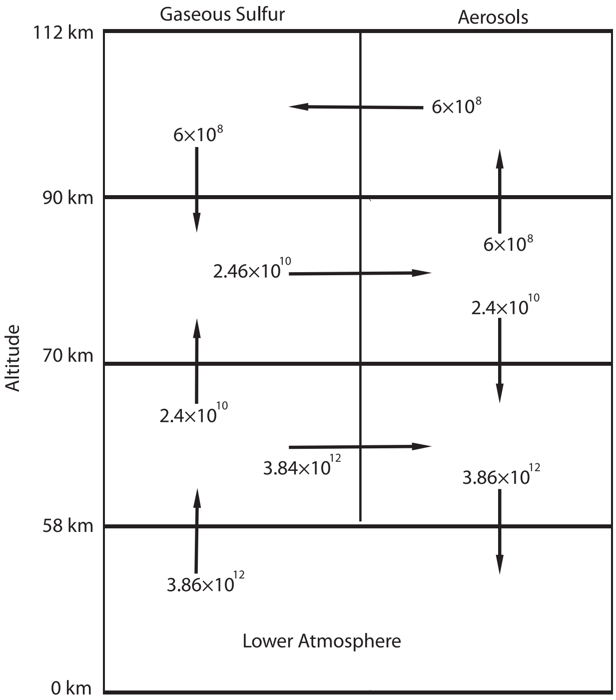

Fig. 16. Sulfur flux flow (in units of cm^{-2} s^{-1}) in the upper atmosphere of Venus.

H_2SO_4 mixing ratio is found to be 3 ppb (~10^6 cm^{-3}), which is two orders of magnitude less than the H_2SO_4 abundance required by Zhang et al. (2010).

Laboratory measurements:

(2) Measurements of photodissociation cross section of H_2SO_4 in the UV region, especially in the lower energy range (~195–330 nm).
(3) Laboratory measurements of H_2SO_4 SVP in the lower temperature region (~150–240 K).
(4) Determination of polysulfur reaction coefficients.

Unsolved problems:

(5) An explanation of the longtime variation of SO_2 at the upper cloud top ~70 km and the possible variation of the OCS abundance in the upper cloud region.
(6) The microphysical properties of S_x and H_2SO_4 aerosols, their formation and loss processes, transport, vertical profiles and the cause of the multi-modal distributions.
(7) Coupled mesosphere-thermosphere (~58–135 km) chemistry including the neutral species and ions to reveal the role of SSAS transport in both dayside and nightside of Venus.

Acknowledgments

We thank E. Marcq for sharing his latest work with us and for helpful discussions, C. Parkinson, S. Bougher and A. Brecht for providing us the recent VTGCM results, A. Ingersoll and D. Yang for insightful comments, R. Zeng for checking the chemical reaction table, M. Gerstell, M. Line and other members of Yung's group at Caltech for reading the manuscript. We are indebted to T. Clancy for pointing out the importance of S_x aerosols as a potential source of SO_2 in the mesosphere of Venus. We acknowledge two anonymous reviewers for their helpful comments. This research was supported by NASA grant NNX07AI63G to the California Institute of Technology. M. C. Liang was funded by NSC Grant 98-2111-M-001-014-MY3 to Academia Sinica. F.P. Mills was supported by grants under the Australian Research Council Discovery Projects and Linkage International schemes. D. A. Belyaev acknowledges support from CNES for a post-doc position at LATMOS.

Appendix A

A.1. Radiative transfer

The diurnally averaged radiation calculation here is modified on the basis of Mills (1998). The direct attenuated flux and Rayleigh scattering calculations remain the same (see details in the Appendix H, and I of Mills (1998)). In this study we adopt 550 log-linear optical depth grids, 112 wavelengths from 960 to 8000 Å, 14 zenith angles for the incoming photons, 8 Gaussian angles for the diffused photons. The wavelength-independent middle cloud albedo at the lower boundary is assumed to be 0.6. The depolarization factor of CO_2 Rayleigh scattering equals 0.443.

The absorption of the unknown UV absorber and scattering processes of haze and cloud particles are crucial for the radiation field, especially in the upper cloud layer. We follow the procedure described in Crisp (1986). First, we calculated the optical depths from the bimodal aerosol profiles (see Appendix B) and scaled to match the optical depth values in Table 2 (equatorial cloud model) of Crisp (1986). Aerosol optical properties are calculated using Mie-code based on the parameters of equator hazes in Table 1 of Crisp (1986). For mode 1, the refractive index is 1.45, radius 0.49 ± 0.22 μm. For mode 2, the refractive index is 1.44, radius 1.18 ± 0.07 μm. Fig. A1 shows the scattering efficiencies (upper panel) and asymmetry factors (middle panel) of the two modes. Since the asymmetry factors do not vary with wavelength significantly, we choose 0.74 as the mean value for all wavelengths. The UV absorber is introduced by decreasing the single scattering albedo of the mode 1 aerosol between 3100 and 7800 Å. We take the empirical absorption efficiency values from Table 4 of Crisp (1986). Fig. A1 (lower panel) shows the single scattering albedo of the mode 1 aerosol mixed with the UV absorber. Because the single

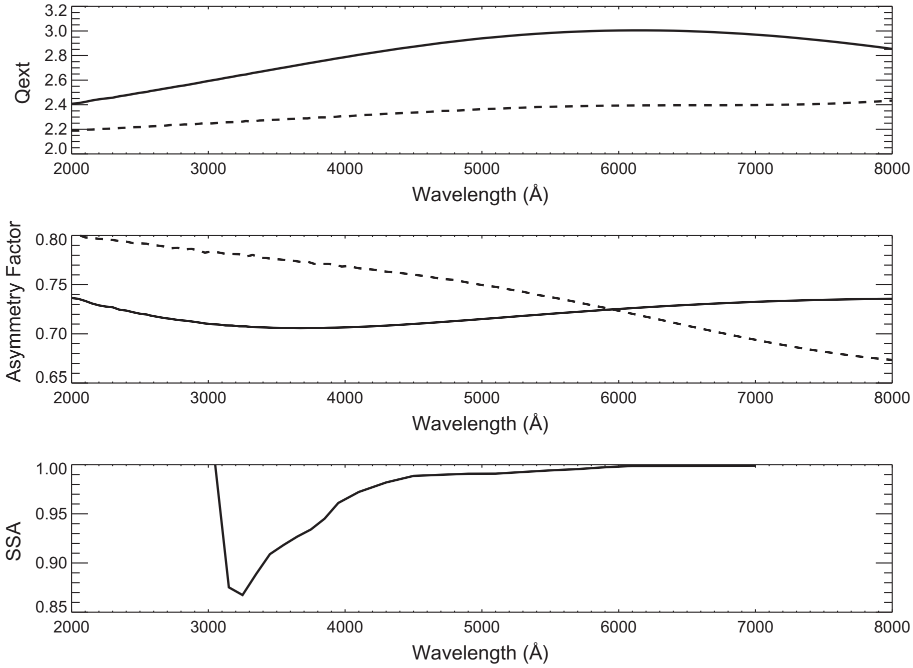

Fig. A1. Optical properties of mode 1 (solid) and mode 2 (dashed) aerosols above the middle cloud top (~58 km) based on the parameters from Crisp (1986). Upper panel: extinction efficiency; Middle panel: asymmetry factor; Lower panel: single scattering albedo mixed with the empirical albedo of the unknown UV absorber from Crisp (1986).

scattering albedo is not constant (from 0.85 to 1) with wavelength, we use the wavelength-dependent values in the calculation. The spectral actinic fluxes (in units of photons cm^{-2} s^{-1} $Å^{-1}$) for 58, 70 and 112 km at 45°N are plotted as functions of wavelength in Fig. A2, although in this study our calculation is at 70°N only. Due to absorptions by CO_2, SO_2 and SO, the UV flux decreases rapidly as it penetrates deeper into the atmosphere. Rayleigh scattering and aerosol scattering result in the larger actinic flux in the cloud and haze layers than that at the top of the atmosphere. In the wavelength range large than 2000 Å, the actinic flux peaks around ~65 km. The UV actinic flux at the lower boundary (~58 km) between 2000 and 3000 Å is roughly anti-correlated with the SO_2 cross sections and the minimum in its the cross section profile near 2400 Å may open a window for the UV flux to penetrate to the lower atmosphere of Venus. There is an analogous spectral window in the terrestrial atmosphere between 200 and 220 nm (Froidevaux and Yung, 1982).

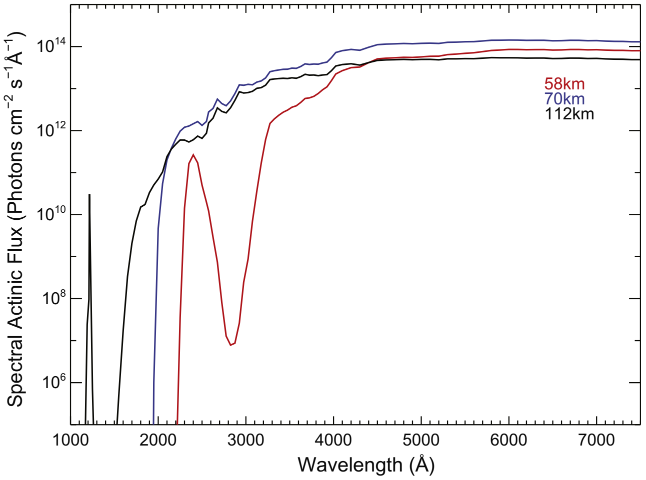

Fig. A2. Spectral actinic flux in the middle atmosphere of Venus at 45°N.

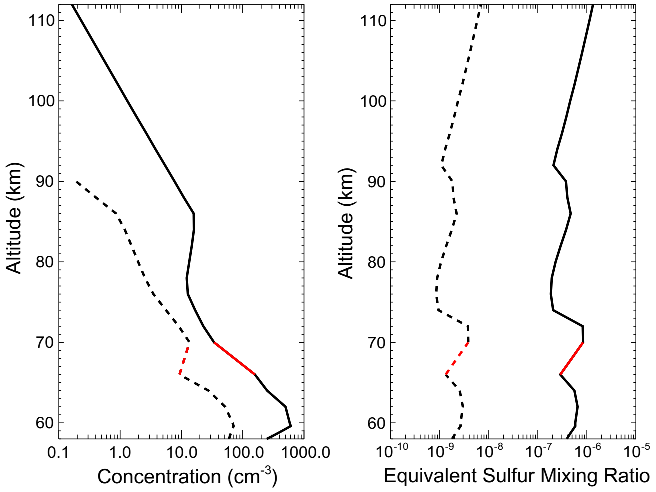

Fig. A3. Left panel: concentration profiles of mode 1 (solid) and mode 2 (dashed) aerosols based on the upper haze profiles from Wilquet et al. (2009) above 72 km and upper cloud particle profiles from Knollenberg and Hunten (1980) from 58 to 65 km. Data are not available in the red region (~66–70 km). Right panel: the equivalent sulfur mixing ratio (ESMR) by volume computed from the H_2SO_4 aerosol (solid line) and the polysulfur aerosol (dashed line). See the text for details. (For interpretation of the references to colour in this figure legend, the reader is referred to the web version of this article.)

Appendix B

B.1. Nucleation rate of elemental sulfur

B.1.1. Aerosol profile

Above the middle cloud top (~58 km), the aerosols are found to exhibit a bimodal distribution in the upper cloud layer (58–70 km) and upper haze layer (70–90 km). In this study we combine the upper haze profiles from Wilquet et al. (2009) above 72 km and upper cloud particle profiles from Knollenberg and Hunten (1980) from 58 to 65 km. Due to the lack of data for the intermediate altitudes (65–72 km) at present, interpolation is applied. Fig. A3 shows the bimodal aerosol profiles (left panel).

From the aerosol abundances, we can estimate the sulfur content. Mode 1 aerosols are ~0.2 μm in radius constantly for all altitudes. For mode 2 aerosols, we use 0.7 μm above 72 km (Wilquet et al., 2009) for the haze particles and 1.1 μm below for the cloud particles (Knollenberg and Hunten, 1980). The right panel in Fig. A3 shows the equivalent sulfur mixing ratio (ESMR) by volume computed from the H_2SO_4 aerosol (solid line) abundances by assuming that the H_2SO_4 aerosol density is 2 g cm^{-3} and weight percent are 85% and 75% below and above 72 km, respectively. The ESMR in the H_2SO_4 droplet is close to 1 ppm at all altitudes, which is enough for the enhancement of sulfur oxides above 80 km. By assuming that the radius of elemental sulfur is about half of the H_2SO_4 aerosol radius and the density is also 2 g cm^{-3}, we found the ESMR in elemental sulfurs in excess of 1 ppb level at most altitude (Fig. A3, right panel, dashed line).

B.1.2. Heterogeneous nucleation

The nucleation rate of elemental sulfurs onto H_2SO_4 droplets is estimated as follows. The nucleation rate constant in the continuum regime (where the particle size is much larger than the vapor mean free path λ) is expressed as (Seinfeld and Pandis, 2006): $J_c = 4\pi R_p D_s$, where R_p is the H_2SO_4 aerosol radius and D_s the molecular diffusivity of elemental sulfur vapor.

However, in the Venus cloud layer, the Knudsen Number K_n ($=\lambda/R_p$) of S_x vapor is not far from 1, so the nucleation process lies in the transition regime where the mean free path λ of the diffusing vapor molecule (e.g., S_x vapor) is comparable to the pre-existing aerosol size. Therefore, we adopt the Dahneke approach (Dahneke, 1983), which matches the fluxes of continuum regime ($K \ll 1$) and free molecular regime ($K_n \gg 1$) by introducing a function $f(K_n)$:

$$f(K_n) = \frac{1+K_n}{1+2K_n(1+K_n)/\alpha} \tag{A1}$$

where α is the molecular accommodation coefficient, which is the probability of sticking when the vapor molecule encounters a particle. Here the mean free path λ in K_n is defined as $2D_s/v$, where v is the mean thermal velocity of the vapor molecule.

Finally we obtain the nucleation rate constant:

$$J = f(K_n)J_c = \frac{4\pi R_p D_s(1+K_n)}{1+2K_n(1+K_n)/\alpha} \tag{A2}$$

The molecular diffusivity D_s of sulfur vapor can be estimated using hard sphere approximation: $D_s = b/N$, where N is the total CO_2 gas density in the environment and b is the binary collision parameter:

$$B = \frac{3}{4\pi(d_s+d_g)^2}\left(\frac{2\pi kT(m_s+m_g)}{m_s m_g}\right)^{1/2} \tag{A3}$$

where d_s and d_g are the diameters of S_x and CO_2 molecule, respectively (assuming $d_s = d_g = 3$ Å), k is the Boltzmann constant, T is the temperature, m_s and m_g are the mass of S_x and CO_2 molecule, respectively. Fig. 15 shows the total nucleation timescale of S_2

calculated from two modes of aerosols (roughly the same for other allotropes), together with the eddy transport timescale and photolysis timescales of S_2, S_3 and S_4. See the discussion in Section 4.

Appendix C

C.1. H_2SO_4 and S_x vapor abundances

C.1.1. H_2SO_4

If sulfuric acid is in thermodynamic equilibrium with the surrounding atmosphere, the saturation vapor pressure (SVP) over H_2SO_4 aerosol should mainly depend on the temperature and aerosol composition. However, non-thermodynamic equilibrium in the real atmosphere is common because the chemical and dynamic processes, such as the chemical production, loss, condensation, evaporation and transport, are often involved and play important roles. The condensation efficiency, which depends on many microphysical properties of the system like the temperature, diffusivity, aerosol size, surface tension, and interaction between molecules and aerosols, will greatly affect the H_2SO_4 vapor pressure over the liquid droplets. The very low condensation rate could cause large supersaturation of the H_2SO_4 vapor. For example, the saturation ratio of H_2SO_4 in the lower stratospheric sulfate layer (Junge layer) on Earth has been observed to be as large as 10^2–10^3 (Arnold, 2006). A similar situation may exist in the Venus upper haze layer on the dayside when the H_2SO_4 vapor on the night side is transported to the dayside, because the SVP of H_2SO_4 in the night side is several orders of magnitude larger than that in the dayside (Zhang et al., 2010) due to the large temperature difference above 90 km. Zhang et al. (2010) proposed that this might be the key mechanism to explain the SO_2 inversion layer because the nighttime H_2SO_4 abundance could be enough to produce the observed SO_2 under photochemical processes if the H_2SO_4 photolysis cross section is 100 time larger than the current data from Vaida et al. (2003).

In the condensation processes, we assume that the sulfate aerosol will quickly establish equilibrium with respect to water because there are more collisions of aerosol particles with H_2O molecules than with H_2SO_4 molecules. Therefore, we could derive the H_2SO_4 aerosol composition (weight percent) from the water activity (or equilibrium relative humidity) defined as the partial pressure of water vapor divided by the SVP over pure water under the same temperature. The water activity is shown in Fig. A4 (left panel) for day and night temperature profile, respectively. We used the H_2O SVP as function of temperature from Tabazadeh et al. (1997), which is valid between 185 and 260 K.

$$P_{H_2O} = \exp\left(18.4524 - \frac{3.5052\times10^3}{T} - \frac{3.3.92\times10^5}{T^2} - \frac{1.2725\times10^7}{T^3}\right) \tag{A4}$$

where P_{H_2O} is the SVP of H_2O in mbar and T is temperature. We extrapolated the formula to the entire temperature range (156–274 K) of Venus mesosphere so there would be some uncertainties above 84 km for the dayside temperature and in the 84–90 km for the nightside.

The H_2SO_4 weight percent is roughly estimated by comparing the observed H_2O mixing ratio profile with the theoretical profiles under different H_2SO_4 compositions, as shown in Fig. A4 (the middle and right panels). For the 50–80 wt.% H_2SO_4, we computed the H_2O mixing ratio profiles based on Clegg and Brimblecombe (1995) and Tabazadeh et al. (1997). For the more concentrated acids, our calculation is based on Gmitro and Vermeulen (1964) although it may not be very accurate for the low temperature (Mills, 1998). There are also some uncertainties in applying the Tabazadeh et al. (1997) formula to Venus because the Clegg and Brimblecombe (1995) is only valid if the water activity larger than 0.01. The atmosphere of Venus is very dry (Fig. A4), and so actually only the results in the region from 85 to 100 km in the dayside and 85–90 km in the nightside seem robust. However, as we showed before, the H_2O SVP may have some uncertainties in those regions. Therefore, the H_2SO_4 weight percent derived here is only a rough estimate based on the current knowledge.

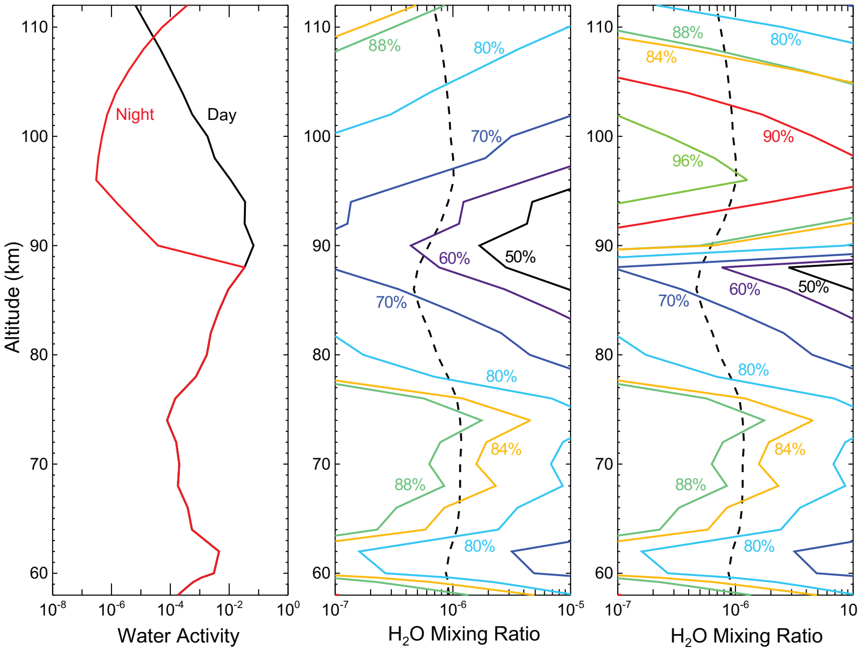

Fig. A4. Left panel: water activity profiles based on the daytime and nighttime temperature profiles. Middle and right panels: equilibrium H_2O mixing ratio contours from which H_2SO_4 weight percent for each altitude could be inferred by comparing the observed H_2O profile (dashed line). The middle and right panels are for the day and night temperature situations, respectively.

The H_2SO_4 weight percent falls with altitude, associated with the increase of relative humidity due to the temperature decrease. The values are about 90–84% in 58–70 km and 84–60% in 70–90 km, which are roughly consistent with the H_2SO_4 compositions obtained from aerosol refractive indexes based on the photometry measurements (85% and 75%, respectively). But in the region above 90 km, the large contrast of dayside and nightside temperatures results in large difference of the local H_2SO_4 weight percent. For example, H_2SO_4 at 100 km is ~75% in the dayside but can be larger than 96% in the nightside if the H_2O vapor profiles are the same for both hemispheres. Actually the temperature profile above 90 km has been found to be a function of longitude (Bertaux et al., 2007). Therefore, if the transport is efficient, the H_2SO_4 aerosols could have a broad range distribution of various concentrations above 90 km but the H_2SO_4 vapor abundances might be mainly determined by the warmest nightside temperature since the vapor abundances is extremely sensitive to the temperature.

The H_2SO_4 SVP is another uncertainty and maybe the major one. In the supplementary material of Zhang et al. (2010), three H_2SO_4 SVP formulas as function of temperature and H_2SO_4 concentration have been discussed in details. These formulas could differ by several orders of magnitude but none of them has been verified in the temperature range of upper atmosphere of Venus. Instead of using the H_2SO_4 weight percent profile derived in Fig. A4, we simply assumed 85% H_2SO_4 below 70 km and 75% from 70 to 90 km and used the vapor pressure formulas from Ayers et al. (1980) corrected by Kulmala and Laaksonen (1990):

$$\ln P^0_{H_2SO_4} = 16.259 + \frac{\mu - \mu_0}{8.3143T} + 10156 \times \left(\frac{1}{T} + \frac{0.38}{T_c - T_0}\left(1 + \ln\left(\frac{T_0}{T}\right) - \frac{T_0}{T}\right)\right) \quad \text{(A5)}$$

where T_c = 905 K, T_0 = 360.15 K, $P^0_{H_2SO_4}$ is SVP of H_2SO_4 in atm, T is the temperature, μ and μ_0 are the chemical potentials of H_2SO_4 solutions of certain composition and pure acid, respectively. The values of μ–μ_0 for the 85% and 75% H_2SO_4 are, respectively, 1555 cal^{-1} mole and 3681 cal^{-1} mole based on Giauque et al. (1960).

In fact the H_2SO_4 abundances in the region below 80 km are not important because the H_2SO_4 photolysis is negligible for the lower region chemistry. But in the upper region the H_2SO_4 might behave like a sulfur source rather than a sink, and large abundance of H_2SO_4 is required in the upper region in order to reproduce the SO_2 inversion layer (Zhang et al., 2010). So we adopted the formula by Stull (1947) just for reference, simply because it gives the largest SVP in the Venus temperature range:

$$P_{H_2SO_4} = 10^{-3954.90/T + 9.4570} \quad \text{(A6)}$$

where $P_{H_2SO_4}$ is the SVP of H_2SO_4 in mmHg and T is temperature. The H_2SO_4 SVP profiles in Fig. A5 (left panel) show large difference between the dayside and nightside caused by the difference in temperatures. Since H_2SO_4 is very hygroscopic, the right panel shows the abundance of monohydrate ($H_2SO_4 \cdot H_2O$), estimated based on the extrapolation of the equilibrium constants from the Vaida et al. (2003) for the Earth atmosphere (223–271 K in the literature). The abundances of $H_2SO_4 \cdot H_2O$ above 90 km are less than 5% and much less ($<10^{-5}$) of that of pure H_2SO_4 for the dayside and nightside, respectively, although the equilibrium constants have not been verified in the Venus temperature region (~160–240 K).

C.1.2. S_x

Lyons (2008) summarized the previous laboratory measurements and computed vapor pressure over the liquid sulfur allotropes and the total solid sulfur vapor pressures over the orthorhombic sulfur and the monoclinic sulfur below the melting points. Based on the data, the author estimated the equilibrium vapor pressure over solid sulfur allotropes. In this study, we follow the same method and calculated the monoclinic S_x saturated volume mixing ratio profiles under the daytime and nighttime temperature situations. The results are shown in Fig. A6.

Appendix D

D.1. Photolysis cross section

H_2SO_4 was thought to be photodissociated by the UV photons only. Burkholder et al. (2000) and Hintze et al. (2003) estimated the upper limits for the UV cross section of H_2SO_4 based on the failure to detect any absorption beyond 140 nm. The upper limits are

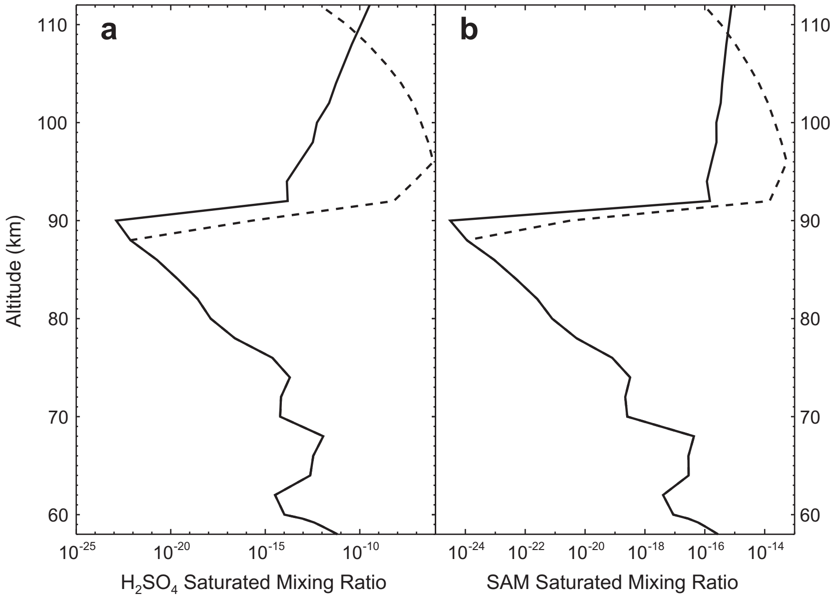

Fig. A5. Left panel: H_2SO_4 vapor volume mixing ratio profiles in equilibrium with the daytime (solid) and nighttime temperatures (dashed). Right panel: monohydrate ($H_2SO_4 \cdot H_2O$) vapor volume mixing ratio profiles.

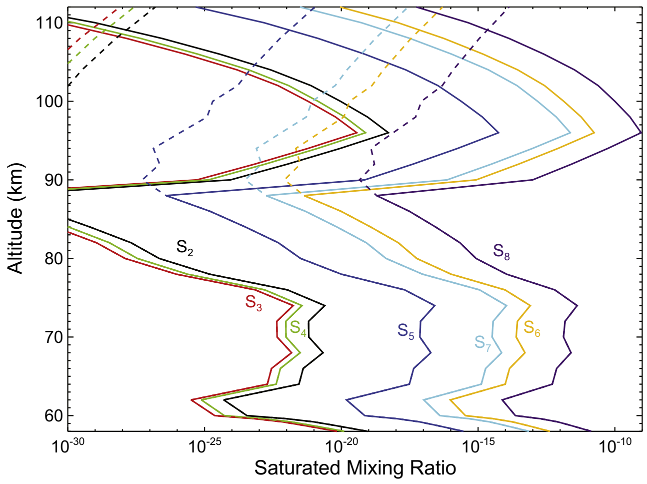

Fig. A6. Saturated vapor volume mixing ratio profiles of S_x allotropes based on the monoclinic S_x saturated vapor pressure over solid S_x based on Lyons (2008), in equilibrium with the daytime (dashed) and nighttime (solid) temperatures.

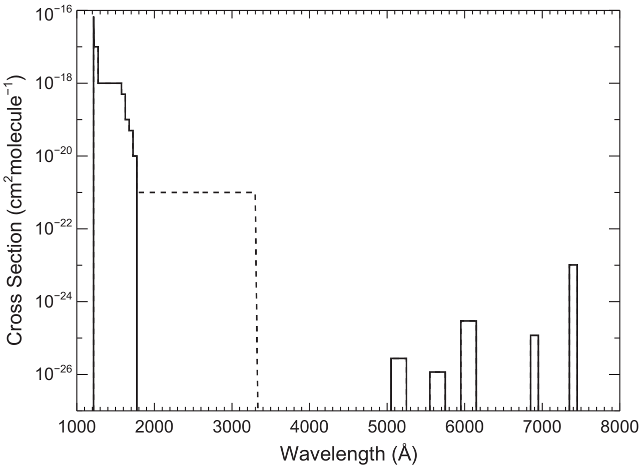

Fig. A7. H_2SO_4 cross sections binned in the model grids. Solid: data from Lane and Kjaergaard (2008) for the UV region, and Mills et al. (2005) and Feierabend et al. (2006) for the visible region. Dashed: same as the solid line but also with 1×10^{-21} cm^2 molecule^{-1} in the UV region of 195–330 nm.

assumed to be 1×10^{-21} cm^2 molecule^{-1} in the interval 195–330 nm, 1×10^{-19} cm^2 molecule^{-1} in 160–195 nm, and 1×10^{-18} cm^2 molecule^{-1} in 140–160 nm. Lane and Kjaergaard (2008) revisited the UV cross sections by calculating the electronic transitions based on the theoretical twin hierarchial approach and they found that the cross section in the Lyman-α region (~121.6 nm) is about $\sim 6 \times 10^{-17}$ cm^2 molecule^{-1}, much larger than the previously assumed value. And it also seems that the cross section in the interval 195–330 nm is much smaller than the upper limits from Burkholder et al. (2000).

Vaida et al. (2003) proposed that in the visible region the excitation of the OH-stretching overtone transitions with $v \geqslant 4$ (~38.6 kcal mole^{-1}, or ~742 nm) is also enough to photolyze H_2SO_4 because the energy required for $H_2SO_4 + h\upsilon \rightarrow SO_3 + H_2O$ is only 32–40 kcal mole^{-1}. This mechanism has been verified by the laboratory experiments in $4\upsilon_9$ and $5\upsilon_9$ bands from the cavity ring-down spectroscopy by Feierabend et al. (2006). Vaida et al. (2003) also proposed that, in the IR and visible regions the OH-stretching overtone transitions with $v \geqslant 3$ (~26.3 kcal/mol, or ~1.09 μm) are able to generate the photodissociation of $H_2SO_4{\cdot}H_2O$ as well (required energy ~25 kcal mole^{-1}) and the total photolysis coefficient is about ~100 times larger than that of pure H_2SO_4, although a recent simulation by Miller and Gerber (2006) suggested that the $H_2SO_4{\cdot}H_2O$ is more likely to thermally decompose to H_2SO_4 and H_2O before photodissociation.

The solid line in Fig. 2 shows the cross sections from Lane and Kjaergaard (2008) for the UV region and Mills et al. (2005) and Feierabend et al. (2006) data for the visible region and binned in our model spectral grid. As shown in Table 1, the H_2SO_4 photolysis coefficient is generally $\sim 10^{-7}$ s^{-1} in the upper atmosphere. It is $\sim 10^{-6}$ s^{-1} near the upper boundary (112 km) due to the photolysis by the Lyman-α line but only in a very thin layer (<1 km) because the Layman alpha intensity decreases very rapidly due to the CO_2 absorption. The major contribution to the photolysis is the solar pumping of the vibrational overtones by the 740 nm red light ($4\upsilon_9$ band, Vaida et al., 2003). The collisional deactivation mainly depends on the atmospheric pressure. In Miller et al. (2007) the quantum yield is nearly unity above 60 km where the pressure is 0.2 mbar in the Earth atmosphere. In Venus, this pressure level (0.2 mbar) is at ~90 km which is the lower boundary of the H_2SO_4 photolysis region we are interested here. Therefore the quantum yield is assumed to be unity above 90 km.

However, Zhang et al. (2010) showed that the photolysis coefficient $\sim 10^{-7}$ s^{-1} is not enough to produce the observed SO_2, otherwise a very large supersaturation of H_2SO_4 (~100) under nighttime temperature is needed. Although this supersaturation is possible (as seen in Earth), empirically they also found the required cross section is about ~100 times larger than that of pure H_2SO_4 if keeping the H_2SO_4 vapor abundances roughly the same as the nighttime saturated abundances. This extreme situation may suggest the existence of large amount of $H_2SO_4{\cdot}H_2O$ and maybe other hydrates (like $H_2SO_4{\cdot}2H_2O$), although it seems not very likely not only because the equilibrium abundance of the monohydrate is small (see Fig. A5) but also because the sulfuric acid hydrates might readily condense into the crystal phase even under the nighttime temperature (McGouldrick et al., 2010). Alternatively, the required large cross section actually could be achieved by assuming the UV cross section as the upper limit of 1×10^{-21} cm^2 molecule^{-1} between 195 and 330 nm, as shown in dashed line in Fig. A7. We consider this possibility in the model A. Note that this change of H_2SO_4 photolysis may not affect much for the Earth stratosphere below 35 km because of the absorption of O_3 Hartley band dominates the actinic flux in that region. However, this is very important for the Venus mesosphere above the cloud top since the SO_2 absorption is not as strong as O_3. The H_2SO_4 photolysis coefficient in this case is $\sim 8.3 \times 10^{-6}$ s^{-1} at 90 km, roughly the same as that of $\sim 8.2 \times 10^{-6}$ s^{-1} if we use the $H_2SO_4{\cdot}H_2O$ photolysis cross section instead (model B in Zhang et al. (2010)).

References

Arnold, F., 2006. Atmospheric aerosol and cloud condensation nuclei formation: A possible influence of cosmic rays? Space Sci. Rev. 125, 169–186.

Atkinson, R., Baulch, D.L., Cox, R.A., Hampson Jr., R.F., Kerr, J.A., Troe, J., 1989. Evaluated kinetic and photochemical data for atmospheric chemistry: Supplement III. J. Phys. Chem. Ref. Data 18 (3), 881–1097.

Atkinson, R. et al., 2004. Evaluated kinetic and photochemical data for atmospheric chemistry: Volume I – Gas phase reactions of O_x, HO_x, NO_x and SO_x species. Atmos. Chem. Phys. 4, 1461–1738.

Ayers, G.P., Gillett, R.W., Gras, J.L., 1980. On the vapor pressure of sulfuric acid. Geophys. Res. Lett. 7, 433–436.

Bahou, M., Chung, C.Y., Lee, Y.P., Cheng, B.M., Yung, Y.L., Lee, L.C., 2001. Absorption cross sections of HCl and DCl at 135-232 nanometers: Implications for photodissociation on Venus. Astrophys. J. Lett. 559, L179–L182.

Baulch, D.L., Duxbury, J., Grant, S.J., Montague, D.C., 1981. Evaluated kinetic data for high temperature reactions. Volume 4 homogeneous gas phase reactions of halogen- and cyanide-containing species. J. Phys. Chem. Ref. Data, 1–721.

Baulch, D.L. et al., 1992. Evaluated kinetic data for combustion modelling. J. Phys. Chem. Ref. Data 21, 411–734.

Belyaev, D. et al., 2008. First observations of SO_2 above Venus' clouds by means of Solar Occultation in the Infrared. J. Geophys. Res. 113, E00B25. doi:10.1029/2008JE003143.

Belyaev, D., Montmessin, F., Bertaux, J.L., Mahieux, A., Fedorova, A., Korablev, O., Marcq, E., Yung, Y.L., Zhang, X., 2012. Vertical profiling of SO_2 and SO above Venus' clouds by SPICAV/SOIR Solar Occultations. Icarus 217 (2), 740–751.

Bertaux, J.L. et al., 2007. A warm layer in Venus' cryosphere and high-altitude measurements of HF, HCl, H_2O and HDO. Nature 450, 646–649.

Brune, W.H., Schwab, J.J., Anderson, J.O., 1983. Laser magnetic resonance, resonance fluorescence, and resonance absorption studies of the reaction kinetics of $O + OH \rightarrow H + O_2$, $O + HO_2 \rightarrow OH + O_2$, $N + OH \rightarrow H + NO$, and $N + HO_2 \rightarrow$ products at 300 K between 1 and 5 torr. J. Phys. Chem. A 87, 4503–4514.

Bryukov, M.G., Kachanov, A.A., Timonnen, R., Seetula, J., Vandoren, J., Sarkisova, O.M., 1993. Kinetics of HNO reactions with O_2 and HNO. Chem. Phys. Lett. 208, 392–398.

Burkholder, J.B., McKeen, S., 1997. UV absorption cross sections for SO_3. Geophys. Res. Lett. 24, 3201–3204.

Burkholder, J.B., Mills, M., McKeen, S., 2000. Upper limit for the UV absorption cross sections of H_2SO_4. Geophys. Res. Lett. 27, 2493–2496.

Campbell, I.M., Thrush, B.A., 1967. The recombination of nitrogen atoms and the nitrogen afterglow. Proc. R. Soc. Lond. B. Biol. Sci. 296, 201–221.

Carlson, R.W., 2010. Venus' Ultraviolet Absorber and Sulfuric Acid Droplets. International Venus Conference, Aussois, France, 4-4.

Chase, M.W., Davies, C.A., Downey, J.R., Frurip, D.J., McDonald, R.A., Syverud, A.N., 1985. JANAF thermochemical tables. Third edition. I, Al–Co. II, Cr–Zr. J. Phys. Chem. Ref. Data 14 (Suppl.), 1–1856.

Clancy, R.T., Sandor, B., Moriarty-Schieven, G., 2008. Venus upper atmospheric CO, temperature, and winds across the afternoon/evening terminator from June 2007 JCMT sub-millimeter line observations. Planet. Space Sci. 56, 1344–1354.

Clegg, S.L., Brimblecombe, P., 1995. Application of a multicomponent thermodynamic model to activities and thermal properties of 0–40 mol kg^{-1} aqueous sulfuric acid from less than 200 K to 328 K. J. Chem. Eng. Data 40, 43–64.

Connes, P., Connes, J., Benedict, W.S., Kaplan, L.D., 1967. Traces of HCl and HF in atmosphere of Venus. Astrophys. J. 147, 1230–1237.

Crisp, D., 1986. Radiative forcing of the Venus mesosphere 1. Solar fluxes and heating rates. Icarus 67, 484–514.

Dahneke, B., 1983. Simple kinetic theory of Brownian diffusion in vapors and aerosols. In: Meyer, R.E. (Ed.), Theory of Dispersed Multiphase Flow. Academic Press, New York, pp. 97–133.

de Pater, I., Roe, H., Graham, J.R., Strobel, D.F., Bernath, P., 2002. Detection of the forbidden SO $a^1\Delta \rightarrow X^3\Sigma^-$ rovibronic transition on Io at 1.7 μm. Icarus 156, 296–301.

DeMore, W.B. et al., 1994. Chemical Kinetics and Photochemical Data for Use in Stratospheric Modeling: Evaluation Number 11.

DeMore, W.B. et al., 1997. Chemical Kinetics and Photochemical Data for Use in Stratospheric Modeling: Evaluation Number 12.

Dodonov, A., Zelenov, V., Strunin, V., Talroze, V., 1981. Mass-spectrometric determination of rate constants of reaction steps 7. Flow-rate and contact time in the mass-spectrometric probing of a diffusional cloud in a flow. Kinet. Catal. 22, 689–697.

Feierabend, K.J., Havey, D.K., Brown, S.S., Vaida, V., 2006. Experimental absolute intensities of the 4v(9) and 5v(9) O–H stretching overtones of H_2SO_4. Chem. Phys. Lett. 420, 438–442.

Froidevaux, L., Yung, Y.L., 1982. Radiation and chemistry in the stratosphere: Sensitivity to O_2 absorption cross sections in the Herzberg continuum. Geophys. Res. Lett. 9, 854–857.

Giauque, W.F., Hornung, E.W., Kunzler, J.E., Rubin, T.R., 1960. The thermodynamic properties of aqueous sulfuric acid solutions and hydrates from 15-degrees K to 300-degrees K. J. Am. Chem. Soc. 82, 62–70.

Glaze, L.S., Baloga, S.M., Wimert, J., 2010. Volcanic eruptions from linear vents on Earth, Venus and Mars: Comparisons with central vent eruptions. Lunar Planet. Sci. 41, 1147–1148 (abstract).

Gmitro, J.I., Vermeulen, T., 1964. Vapor–liquid equilibria for aqueous sulfuric acid. AIChE J. 10, 740–746.

Grillo, A., Reed, R., Slack, M.W., 1979. Infrared measurements of sulfur-dioxide thermal-decomposition rate in shock-waves. J. Chem. Phys. 70, 1634–1636.

He, Y., Liu, X., Lin, M.C., Melius, C.F., 1993. Thermal reaction of HNCO with NO_2 at moderate temperatures. Int. J. Chem. Kinet. 25, 845–863.

Hermans, C., Vandaele, A.C., Fally, S., 2009. Fourier transform measurements of SO_2 absorption cross sections: I. Temperature dependence in the 24000–29000 cm^{-1} (345–420 nm) region. J. Quant. Spectrosc. Radiat. Transfer 110, 756–765.

Hintze, P.E., Kjaergaard, H.G., Vaida, V., Burkholder, J.B., 2003. Vibrational and electronic spectroscopy of sulfuric acid vapor. J. Phys. Chem. A 107, 1112–1118.

Knollenberg, R.G., Hunten, D.M., 1980. The microphysics of the clouds of Venus: Results of the Pioneer Venus particle size spectrometer experiment. J. Geophys. Res. 85, 8039–8058.

Krasnopolsky, V.A., 2006. A sensitive search for nitric oxide in the lower atmospheres of Venus and Mars: Detection on Venus and upper limit for Mars. Icarus 182, 80–91.

Krasnopolsky, V.A., 2008. High-resolution spectroscopy of Venus: Detection of OCS, upper limit to H_2S, and latitudinal variations of CO and HF in the upper cloud layer. Icarus 197, 377–385.

Krasnopolsky, V.A., 2010a. Spatially-resolved high-resolution spectroscopy of Venus 1. Variations of CO_2, CO, HF, and HCl at the cloud tops. Icarus 208, 539–547.

Krasnopolsky, V.A., 2010b. Spatially-resolved high-resolution spectroscopy of Venus 2. Variations of HDO, OCS, and SO_2 at the cloud tops. Icarus 209, 314–322.

Krasnopolsky, V.A., 2010c. Venus night airglow: Ground-based detection of OH, observations of O_2 emissions, and photochemical model. Icarus 207, 17–27.

Krasnopolsky, V.A., Pollack, J.B., 1994. H_2O–H_2SO_4 system in Venus' clouds and OCS, CO, and H_2SO_4 profiles in Venus' troposphere. Icarus 109, 58–78.

Kulmala, M., Laaksonen, A., 1990. Binary nucleation of water-sulphuric acid system: comparison of classical theories with different H_2SO_4 saturation vapour pressures. J. Chem. Phys. 93, 696–701.

Lane, J.R., Kjaergaard, H.G., 2008. Calculated electronic transitions in sulfuric acid and implications for its photodissociation in the atmosphere. J. Phys. Chem. A 112, 4958–4964.

Liang, M.C., Yung, Y.L., 2009. Modeling the distribution of H_2O and HDO in the upper atmosphere of Venus. J. Geophys. Res. – Planets 114, E00B28.

Lindzen, R.S., 1981. Turbulence and stress owing to gravity-wave and tidal breakdown. J. Geophys. Res. – Oceans Atmos. 86, 9707–9714.

Lovejoy, E.R., Hanson, D.R., Huey, L.G., 1996. Kinetics and products of the gas-phase reaction of SO_3 with water. J. Phys. Chem. 100, 19911–19916.

Lu, C.W., Wu, Y.J., Lee, Y.P., Zhu, R.S., Lin, M.C., 2003. Experiments and calculations on rate coefficients for pyrolysis of SO_2 and the reaction O + SO at high temperatures. J. Phys. Chem. A 107, 11020–11029.

Lu, C.W., Wu, Y.J., Lee, Y.P., Zhu, R.S., Lin, M.C., 2006. Experimental and theoretical investigation of rate coefficients of the reaction S (3P) + OCS in the temperature range of 298–985 K. J. Phys. Chem. 125, 164329. doi:10.1063/1.2357739.

Lyons, J.R., 2008. An estimate of the equilibrium speciation of sulfur vapor over solid sulfur and implications for planetary atmospheres. J. Sulfur Chem. 29, 269–279.

Marcq, E., Bezard, B., Encrenaz, T., Birlan, M., 2005. Latitudinal variations of CO and OCS in the lower atmosphere of Venus from near-infrared nightside spectro-imaging. Icarus 179, 375–386.

Marcq, E., Encrenaz, T., Bezard, B., Birlan, M., 2006. Remote sensing of Venus' lower atmosphere from ground-based IR spectroscopy: Latitudinal and vertical distribution of minor species. Planet. Space Sci. 54, 1360–1370.

Marcq, E., Bezard, B., Drossart, P., Piccioni, G., Reess, J.M., Henry, F., 2008. A latitudinal survey of CO, OCS, H_2O, and SO_2 in the lower atmosphere of Venus: Spectroscopic studies using VIRTIS-H. J. Geophys. Res. – Planets 113, E00B07. doi:10.1029/2008JE003074.

Marcq, E., Belyaev, D., Montmessin, F., Fedorova, A., Bertaux, J.-L., Vandaele, A.C., Neefs, E., 2011a. An investigation of the SO_2 content of the venusian mesosphere using SPICAV-UV in nadir mode. Icarus 211, 58–69.

Marcq, E., Belyaev, D., Bertaux, J.-L., Fedorova, A., Montmessin, F., 2011b. Long-term monitoring SO_2 above the clouds of Venus using SPICAV-UV in nadir mode. EGU General Assembly 13, EGU2011-2003.

Markiewicz, W.J. et al., 2007. Morphology and dynamics of the upper cloud layer of Venus. Nature 450, 633–636.

McGouldrick, K., Toon, O.B., Grinspoon, D.H., 2010. Sulfuric acid aerosols in the atmospheres of the terrestrial planets. Planet. Space Sci. doi:10.1016/j.pss.2010.05.020.

Miller, Y., Gerber, R.B., 2006. Dynamics of vibrational overtone excitations of H_2SO_4, H_2SO_4-H_2O: Hydrogen hopping and photodissociation processes. J. Am. Chem. Soc. 128, 9594–9595.

Miller, Y., Gerber, R.B., Vaida, V., 2007. Photodissociation yields for vibrationally excited states of sulfuric acid under atmospheric conditions. Geophys. Res. Lett. 34, L16820. doi:10.1029/2007GL030529.

Mills, F.P., 1998. I. Observations and Photochemical Modeling of the Venus Middle Atmosphere. II. Thermal Infrared Spectroscopy of Europa and Callisto. PhD Thesis, California Institute of Technology, pp. 1–277.

Mills, F.P., Allen, M., 2007. A review of selected issues concerning the chemistry in Venus' middle atmosphere. Planet. Space Sci. 55, 1729–1740.

Mills, M.J. et al., 2005. Photolysis of sulfuric acid vapor by visible light as a source of the polar stratospheric CN layer. J. Geophys. Res. 110, D08201. doi:10.1029/2004JD005519.

Mills, F.P., Esposito, L.W., Yung, Y.L., 2007. Atmospheric composition, chemistry, and clouds. In: Esposito, L.W., Stofan, E.R., Cravens, T.E. (Eds.), Exploring Venus as a Terrestrial Planet. American Geophysical Union, Washington, DC, pp. 73–100.

Moses, J.I., Bezard, B., Lellouch, E., Gladstone, G.R., Feuchtgruber, H., Allen, M., 2000. Photochemistry of Saturn's atmosphere II. Effects of an influx of external oxygen I. Icarus 145, 166–202.

Moses, J.I., Zolotov, M.Y., Fegley, B., 2002. Photochemistry of a volcanically driven atmosphere on Io: Sulfur and oxygen species from a Pele-type eruption. Icarus 156, 76–106.

Pätzold, M. et al., 2007. The structure of Venus' middle atmosphere and ionosphere. Nature 450, 657–660.

Pernice, H. et al., 2004. Laboratory evidence for a key intermediate in the Venus atmosphere: Peroxychloroformyl radical. Proc. Natl. Acad. Sci. 101, 14007–14010.

Piccialli, A. et al., 2008. Cyclostrophic winds from the Visible and Infrared Thermal Imaging Spectrometer temperature sounding: A preliminary analysis. J. Geophys. Res. – Planets 113, E00B11. doi:10.1029/2008JE003127.

Pollack, J.B., Dalton, J.B., Grinspoon, D., Wattson, R.B., Freedman, R., Crisp, D., Allen, D.A., Bezard, B., Debergh, C., Giver, L.P., Ma, Q., Tipping, R., 1993. Near-infrared light from Venus nightside – A spectroscopic analysis. Icarus 103, 1–42.

Prinn, R.G., 1975. Venus – Chemical and dynamical processes in stratosphere and mesosphere. J. Atmos. Sci. 32, 1237–1247.

Riley, P.S., Cosic, B., Fontijn, A., 2003. The H + NO recombination reaction over a wide temperature range. Int. J. Chem. Kinet. 35, 374–380.

Sander, S.P. et al., 2002. Chemical Kinetics and Photochemical Data for Use in Atmospheric Studies: Evaluation Number 14. Jet Propulsion Laboratory, California Institute of Technology, Pasadena, CA.

Sander, S.P. et al., 2006. Chemical Kinetics and Photochemical Data for Use in Atmospheric Studies: Evaluation Number 15. Jet Propulsion Laboratory, California Institute of Technology, Pasadena, CA.

Sandor, B.J., Clancy, R.T., Moriarty-Schieven, G., Mills, F.P., 2010. Sulfur chemistry in the Venus mesosphere from SO_2 and SO microwave spectra. Icarus 208, 49–60.

Sandor, B.J., Clancy, R.T., Moriarty-Schieven, G.H., 2012. Upper limits for H_2SO_4 in the mesosphere of Venus. Icarus 217 (2), 839–844.

Seiff, A., 1983. Models of Venus's atmospheric structure. In: Hunten, D.M., Colin, L., Donahue, T.M., Moroz, V.I. (Eds.), Venus. University of Arizona Press, Tucson, Arizona, pp. 1045–1048.

Seinfeld, J.H., Pandis, S.N., 2006. Atmospheric Chemistry and Physics: From Air Pollution to Climate Change. John Wiley & Sons, Inc., New York.

Singleton, D.L., Cvetanovic, R.J., 1988. Evaluated chemical kinetic data for the reactions of atomic oxygen $O(^3P)$ with sulfur-containing-compounds. J. Phys. Chem. Ref. Data 17, 1377–1437.

Smrekar, S.E. et al., 2010. Recent hot-spot volcanism on Venus from VIRTIS emissivity data. Science 328, 605–608.

Sonnabend, G. et al., 2005. A new search for OCS in the middle atmosphere of Venus. Bull. Am. Astron. Soc. 37, 750.

Stull, D.R., 1947. Vapor pressure of pure substances—Inorganic compounds. Ind. Eng. Chem. 39, 540–550.

Sun, F. et al., 2001. Reactions of NH_2 with NO_2 and of OH with NH_2O. J. Phys. Chem. A 105, 6121–6128.

Sundaram, M.S., Mills, F.P., Allen, M., Yung, Y.L., 2011. An initial model assessment of NO_x photochemistry on Venus with heterogeneous oxidation of CO. In: Proceedings of the 10th Australian Space Science Conference, Brisbane, Australia, 119–132.

Tabazadeh, A., Toon, O.B., Clegg, S.L., Hamill, P., 1997. A new parameterization of H_2SO_4/H_2O aerosol composition: Atmospheric implications. Geophys. Res. Lett. 24, 1931–1934.

Vaida, V., Kjaergaard, H.G., Hintze, P.E., Donaldson, D.J., 2003. Photolysis of sulfuric acid vapor by visible solar radiation. Science 299, 1566–1568.

Vandaele, A.C. et al., 2008. Composition of the Venus mesosphere measured by Solar Occultation at Infrared on board Venus Express. J. Geophys. Res. 113, E00B23. doi:10.1029/2008JE003140.

Vandaele, A.C., Hermans, C., Fally, S., 2009. Fourier transform measurements of SO_2 absorption cross sections: II. Temperature dependence in the 29000–44000 cm^{-1} (227–345 nm) region. J. Quant. Spectrosc. Radiat. Transfer 110, 2115–2126.

Von Zahn, U., Krankowsky, D., Mauersberger, K., Nier, A.O., Hunten, D.M., 1980. Venus thermosphere – In situ composition measurements, the temperature profile, and the homopause altitude. Science 203, 768–770.

Wilquet, V. et al., 2009. Preliminary characterization of the upper haze by SPICAV/SOIR Solar Occultation in UV to mid-IR onboard Venus Express. J. Geophys. Res. 114, E00B42. doi:10.1029/2008JE003186.

Woo, R., Ishimaru, A., 1981. Eddy diffusion-coefficient for the atmosphere of Venus from radio scintillation measurements. Nature 289, 383–384.

Yung, Y.L., DeMore, W.B., 1982. Photochemistry of the stratosphere of Venus: Implications for atmospheric evolution. Icarus 51, 199–247.

Yung, Y.L. et al., 2009. Evidence for carbonyl sulfide (OCS) conversion to CO in the lower atmosphere of Venus. J. Geophys. Res. 114, E00B34. doi:10.1029/2008JE003094.

Zhang, X., Liang, M.C., Montmessin, F., Bertaux, J.L., Parkinson, C., Yung, Y.L., 2010. Photolysis of sulphuric acid as the source of sulphur oxides in the mesosphere of Venus. Nat. Geosci. 3, 834–837.